Universiteit
Antwerpen

This item is the archived peer-reviewed author-version of:

Assessing neutral transport mechanisms in aspect ratio dependent etching by means of experiments and multiscale plasma modeling

Reference:
Vanraes Patrick, Parayil Venugopalan Syam, Besemer Matthieu, Bogaerts Annemie.- Assessing neutral transport mechanisms in aspect ratio dependent etching by means of experiments and multiscale plasma modeling
Plasma sources science and technology / Institute of Physics [Londen] - ISSN 1361-6595 - 32:6(2023), 064004
Full text (Publisher's DOI): https://doi.org/10.1088/1361-6595/ACDC4F
To cite this reference: https://hdl.handle.net/10067/1977600151162165141

uantwerpen.be
Institutional repository IRUA

Assessing neutral transport mechanisms in aspect ratio dependent etching by means of experiments and multiscale plasma modeling

Patrick Vanraes[1], Syam Parayil Venugopalan[2], Matthieu Besemer[2], Annemie Bogaerts[1]

[1]*PLASMANT, Department of Chemistry, University of Antwerp, Universiteitsplein 1, 2610 Wilrijk-Antwerp, Belgium*

[2]*ASML, De Run 6665, 5504 DT Veldhoven, Netherlands*

Abstract

Since the onset of pattern transfer technologies for chip manufacturing, various strategies have been developed to circumvent or overcome aspect ratio dependent etching (ARDE). These methods have, however, their own limitations in terms of etch non-idealities, throughput or costs. Moreover, they have mainly been optimized for individual in-device features and die-scale patterns, while occasionally ending up with poor patterning of metrology marks, affecting the alignment and overlay in lithography. Obtaining a better understanding of the underlying mechanisms of ARDE and how to mitigate them therefore remains a relevant challenge to date, for both marks and advanced nodes. In this work, we accordingly assessed the neutral transport mechanisms in ARDE by means of experiments and multiscale modeling for SiO_2 etching with CHF_3/Ar and CF_4/Ar plasmas. The experiments revealed a local maximum in the etch rate for an aspect ratio around unity, i.e. the simultaneous occurrence of regular and inverse reactive ion etching lag for a given etch condition. We were able to reproduce this ARDE trend in the simulations without taking into account charging effects and the polymer layer thickness, suggesting shadowing and diffuse reflection of neutrals as the primary underlying mechanisms. Subsequently, we explored four methods with the simulations to regulate ARDE, by varying the incident plasma species fluxes, the amount of polymer deposition, the ion energy and angular distribution and the initial hardmask sidewall angle, for which the latter was found to be promising in particular. Although our study focusses on feature dimensions characteristic to metrology marks and BEOL integration, the obtained insights have a broader relevance, e.g. to the patterning of advanced nodes. Additionally, this work supports the insight that physisorption may be more important in plasma etching at room temperature than originally thought, in line with other recent studies, a topic on which we recommend further research.

Keywords: Microloading, ARDE, normal RIE lag, inverse RIE lag, Knudsen diffusion, aspect ratio independent etching, plasma etching

1. Introduction

Semiconductor manufacturing involves many processing steps, as portrayed in Figure 1. Photolithography and plasma etching are among the critical patterning procedures involved in this chain of processing steps. In photolithography, light of a suitable wavelength is used to transfer the pattern from a mask (reticle) to a photosensitive resist, coated on the wafer. Subsequently, plasma etching is used to transfer the pattern from the resist to the underlying layers (hardmask, dielectrics and conductors) that make up the integrated circuits. One of the important factors that has historically helped improvement in microprocessor performance is the ability to fabricate smaller and smaller transistors. This is facilitated by advancements in lithography and pattern transfer methods such as plasma etching, also known as reactive ion etching (RIE).

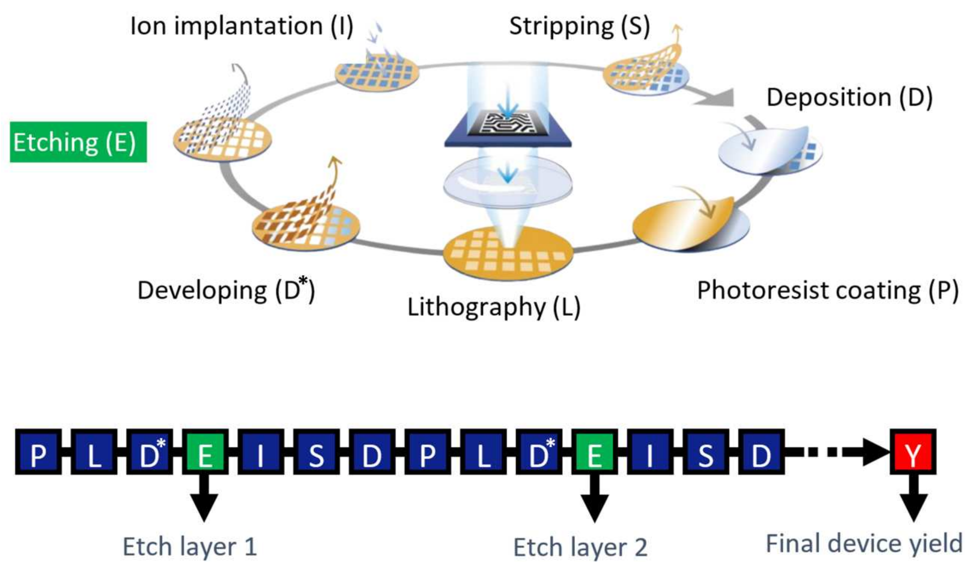

Figure 1. Typical processing steps involved in semiconductor chip manufacturing.

Ideally, during the etching process, it is desired to transfer the etch mask pattern into the underlying layer, leaving vertical sidewalls and a horizontal trench floor. However, etch-induced non-idealities can result in various undesired artifacts such as asymmetric sidewall angles or floor tilt. Such etch-induced asymmetries could lead to alignment and overlay errors of subsequent layers that are built on top of existing layers. Overlay is the measure of how accurate two adjacent layers of the integrated circuit are aligned relative to each other. It is an important metric in semiconductor fabrication, as a poor overlay could result in open contacts or unintended shorts between adjacent layers, thereby severely affecting the device yield [1, 2]. The contribution of ions to etch-induced asymmetries was investigated in one of our earlier publications [3]. The present work will focus on the contribution of neutrals, with special attention to microloading and aspect ratio dependent etching (ARDE).

On the microscopic scale, etch rate non-idealities depend on two mechanisms, namely, microloading and aspect ratio dependent etching (ARDE) as defined by Gottscho et al. [4]. Aspect ratio in this context refers to the ratio of the height (defined in the z-direction) to the width (x/y-direction) of a given feature. ARDE

stems from the observation that the etch rate of a given feature scales with the aspect ratio and changes over time since the aspect ratio increases as time progresses [4, 5]. Gottscho et al. categorized these two mechanisms further into (1) Knudsen transport of neutrals, (2) ion shadowing, (3) neutral shadowing, (4) differential charging of an insulating microstructure, (5) field curvature near the conductive topography, (6) surface diffusion, (7) bulk diffusion, and (8) image force deflection [4]. Of these eight categories, the first four mechanisms are most commonly considered to underlie ARDE, where the first three will be the focus of this work.

Process non-idealities due to ARDE are difficult to overcome and are usually mitigated by influencing the first four categories (Knudsen transport, ion shading, neutral shadowing, and differential charging of an insulating microstructure) by applying changes to the plasma etch conditions.

One of the biggest challenges in ARDE is to control the transport of neutrals and ions to the etch front, while maintaining plasma purity. At the wafer surface level, neutrals can be considered to be in the bulk diffusion regime, having mean free paths ranging from tens of micrometers to a few millimeters, which greatly exceeds the feature sizes. Within the features, neutrals undergo so-called Knudsen diffusion, determined by a constant adsorption and thermal re-emission of neutrals from the sidewalls, where the diffusivity is proportional to the critical dimension (CD), i.e. the width of the trench, resulting in much lower diffusion constants compared to the bulk. In this process, the mean free path of the neutral species is not only determined by the CD, but also temperature, pressure, and the mass of the neutral species [4, 6, 7]. The flux of neutrals toward the etch front can therefore be modified by changing either one of those parameters. On the other hand, the ion flux towards the etch front can be increased by, for example, operating at a higher RF bias power in a capacitively coupled plasma (CCP) reactor or increasing the bias voltage in an inductively coupled plasma (ICP) reactor, thereby affecting the ion energy and angular distribution (IEAD).

ARDE can be further mitigated by balancing the plasma chemistry between two opposing lag regimes: so-called RIE lag and inverse RIE lag [4]. RIE lag refers to the most common manifestation of ARDE where the etch rate declines with increasing aspect ratio. Inverse RIE lag, on the other hand, indicates the opposite effect. The former is often associated with low incident neutral-to-ion flux ratios, whereas the latter more commonly occurs at high ratios [7-10]. In these cases, the neutrals correspond to depositing polymerizing or passivating species that slow down the etch rate (see e.g. [9, 11-15]). A lower flux of such neutrals reaching the bottom of narrow trenches relative to wider ones is therefore often used to explain inverse RIE lag (see e.g. [7, 8, 10, 16, 17]). The transition between regular and inverse RIE lag is namely attributed to a competition between etching and deposition reactions, as well as the much stronger shadowing effect for neutrals in comparison to ions. However, the true origin of inverse RIE lag remains controversial, because it can be caused by multiple mechanisms [10, 16, 18]. For example, a faster etch rate of high aspect ratio features may also be due to the merging of the ion scattering-induced microtrenches at the bottom edges with decreasing CD [10, 14, 16, 18, 19]. In the present work, we will propose an alternative mechanism.

As should also be kept in mind, the Knudsen transport of neutrals toward a trench bottom will differ depending on whether they are subject to chemisorption or physisorption. That is, molecules are more

likely to thermally desorb from the sidewalls and continue their trip to the trench bottom, while radicals first need to passivate the sidewalls to decrease their local sticking probability. At high aspect ratios, the flux at the bottom can thus depend on the reactivity of the species. Furthermore, the deposition at the bottom may be assisted by the incident ions, as already suggested in 1994 by Joubert, Oehrlein and Surendra, in agreement with experimentally observed polymer buildup primarily at a contact base after etch [20, 21]. Moreover, the deposited layer thickness is expected to strongly determine the RIE lag regime, because substrate removal will be the strongest at an optimal thickness for ion-induced chemical etching, whereas it will be delayed for thinner or thicker layers. Each of these effects complicates a profound understanding of the lag regimes and thus the fine-tuning of the plasma chemistry for aspect ratio independent etching.

Other mitigation strategies have been considered and are covered extensively in, for instance, Ref. [4, 6]. Additionally, a common method which integrated circuit manufacturers employ is to partially circumvent ARDE by means of over etch (OE) and employing a stopping layer. Although this strategy of over etch has been proven useful for a better uniformity of functional device features, it can display a worse performance for alignment and overlay marks, for which the etch recipe is often not fine-tuned. In general, etch recipes are namely optimized for individual in-device features in the first place, pattern density dependent uniformity in the second place, and only afterwards for the etch performance of metrology marks [22]. Furthermore, stopping layers never have perfect selectivity, and over etch can result in other undesired effects [23, 24]. Next to that, the stopping layer sometimes is not thick enough or requires a multi-layer stopping layer scheme with a top, middle and bottom [25, 26]. Other methods to almost fully circumvent ARDE make use of a multi-step sequence with alternating deposition and etching [27] or so-called self-limiting techniques, such as atomic layer etching (ALE) and atomic layer deposition (ALD) [28, 29]. Despite the huge potential of ALE and ALD techniques, they are nowadays only used in critical etching steps as these techniques are relatively expensive and lack high throughput. The remediation of ARDE through alternative methods therefore remains a highly relevant topic today. For this purpose, a more fundamental understanding of neutral transport in ARDE will help mapping and driving the etching performance for state-of-the-art technology nodes.

In this work, we study the neutral transport mechanisms in ARDE through plasma etch simulations using a bottom-up designed surface chemistry set of CF_4/CHF_3/Ar plasma over a SiO_2 wafer in a capacitively coupled plasma (CCP) etch reactor. For this purpose, we use a multi-layer stack that is commonly implemented in the back-end-of-the-line (BEOL) processes [25]. A specific technology or application is, however, not considered, in order to retain a broad scope in our investigation. We start from the observation of a local maximum in the etch rate at a CD between 100 and 200 nm, in our supporting experiments, as well as experimental data in the scientific literature [8, 14, 18, 19, 30-32]. Next, we reveal how our simulations qualitatively reproduce this peak, which we attribute to diffuse reflection and thermal desorption of neutrals from the sidewalls. Our hypothesis is verified by modifying the properties of the neutrals' re-emission from the surface in the simulations. Finally, we demonstrate how the peak and normal-lag are affected by experimental conditions, in order to propose a strategy to suppress them.

The paper is organized in the following manner. In section 2, we describe the experimental and simulation methods used to study the plasma etching process, as well as the analysis techniques to quantify ARDE.

Section 3 deals with the first part of the results and their discussion, for the identification of the neutral transport mechanisms underlying ARDE. Section 4 continues on the results and their discussion, but from a more practical perspective on how to regulate ARDE by means of different experimental parameters. In Sections 5 and 6, finally, we discuss the concluding remarks and outlook.

2. Methodology

2.1 Description of the experiments

The experiments have been performed with a Leybold F2 reactor as depicted in Figure 2. This reactor has also been used in our previous work [33], to validate the surface chemistry set in the simulations, as further discussed in Section 2.2. Its settings were kept largely the same as in this prior work, but the CHF_3/Ar gas ratio, pressure and applied power were varied as indicated in Table I. The stack used in the experiments contained an oxide layer on top of a titanium nitride (TiN) stop layer. The oxide layer was patterned with a tri-layer mask containing photoresist (PR), spin-on glass (SOG) and spin-on carbon (SoC), as shown in Figure 2(d). The photoresist, i.e. chemically amplified resist (CAR), was patterned using a deep ultraviolet (DUV) lithography tool. The pattern was transferred to the SoG using a fluorocarbon chemistry in a plasma etch chamber. Subsequently, the pattern was transferred from SoG to SoC using a H_2/N_2-based chemistry. The resulting patterned SoC acts as the etch mask on the oxide layer in our experiments, where the oxide layer serves as the material to be etched. For this reason, the patterned SoC layer will generally be referred to as the etch mask or the hardmask in the remainder of the present paper.

After preparation, the wafers were sliced into coupons and mounted into the Leybold F2 reactor on the center of the bottom electrode, to be processed by means of plasma etching for the operating conditions defined in Table I for an etch time of t_{etch} = 240 s. The self-bias voltage was recorded for an input power of 60 W to be 635 and 506 V at 15 and 45 µbar, and for 90 W to be 819 and 747 V at 15 and 45 µbar, respectively. In order to limit the presence of atmospheric impurities during the etch process, the reactor was operated in a clean room and it was connected to a turbo vacuum pump to bring its pressure near vacuum right before the start of each experiment, after which the chamber was filled with the etch gas. To ensure reproducibility, the process parameters, such as gas flow rates, pressure, and power, were continuously monitored. The bottom electrode was at room temperature before each experiment, but its temperature was not controlled during the etch process. All experiments were performed in duplicate, unless mentioned otherwise. After the plasma processing, the samples were cut in order to investigate the cross section of the etched geometry using SEM imaging. To avoid the influence of boundary effects at the sample edges due to loading or non-uniform temperature profiles, the images were only examined near the center of the coupons. From these cross sections, the corresponding etch depth and average etch rate were determined by means of WebPlotDigitizer (version 4.2), a publically available semi-automated image processing software developed by Ankit Rohatgi [34], as described in more detail in Appendix A.

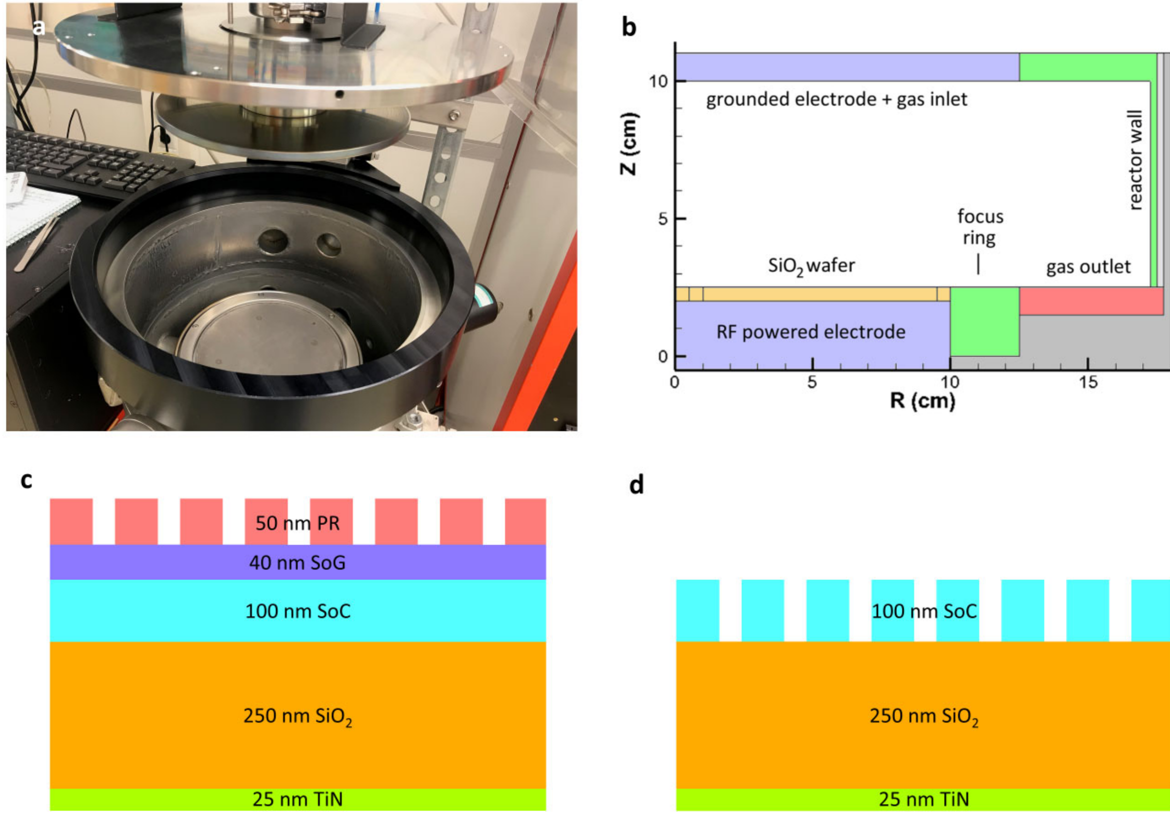

Figure 2. The Leybold F2 reactor and wafer stack. (a) Pictures of the experimental setup. (b) The reactor scheme used in the plasma simulations, where the Z-axis serves as the axisymmetry axis. (c) The wafer stack used in the experiments, in its original unprocessed form and (d) after the preparation steps that transfer the pattern from the photoresist (PR) to the spin-on carbon (SoC) layer. The original stack consists of a TiN stop layer, a deposited SiO_2 layer, a SoC layer, spin-on glass (SoG) layer and the photoresist. (b) Reprinted with permission from [33].

Table I. Operating conditions of the Leybold F2 reactor used for the experiments and simulations in this work. NA stands for not applicable.

Parameter	**Experiments**				**Simulations**
Gas ratio CHF_3/Ar	25/75	25/75	25/75	25/75	NA
Gas ratio CF_4/Ar	NA	NA	NA	NA	10/90
Pressure (µbar)	15	15	45	45	30
Applied power (W)	60	90	60	90	75
Frequency (MHz)	13.56	13.56	13.56	13.56	13.56
Wafer temperature (K)	293	293	293	293	293
Gas flow rate (sccm)	60	60	60	60	60

2.2 Description of the simulations

The plasma etching simulations in the present study have been performed by means of the Hybrid Plasma Equipment Model (HPEM) and the Monte Carlo Feature Profile Model (MCFPM), both of which were developed by the Kushner group [35]. HPEM consists of several modules, each of which handles a different aspect of the plasma etching. This makes it a versatile tool to simulate the plasma on the reactor level in 2D, using axisymmetry. Among its output, it provides the fluxes and the energy and angular distributions of the plasma species incident on the wafer surface, which in turn serve as input for MCFPM. MCFPM operates as a separate kinetic Monte Carlo method, where the evolution of the wafer surface is calculated on the feature level. More specifically, it simulates the incident plasma species as super-particles, i.e. computational particles representing a collection of real, physical plasma species, which are assumed to interact with rectangular material cells that represent the surface structure. The outcome of these interactions is calculated by means of a user-defined surface chemistry set.

As elaborately explained in our previous work [33], we have developed a surface chemistry set that is unique in its kind due to its bottom-up design, for Si or SiO_2 etching by a CF_4/CHF_3/Ar plasma. That is, each interaction in the set between an incident plasma particle and a surface group has been based on quantitative fundamental knowledge on this interaction, obtained from empirical data and/or first-principles simulations. This allows it to be straightforwardly applied for a fundamental analysis. In contrast to the surface chemistry of the substrate material, the surface reactions on the hardmask were kept rudimentary, due to the lack of fundamental data on them. For the present study, the surface chemistry of the etch mask was updated for the neutral plasma species, by assuming all neutral species to diffusely reflect on its surface with a probability of 100%, as further explained in Section 3.2. A more detailed description of HPEM, MCFPM and the surface chemistry set can be found in Refs. [33, 35]. In the Supplementary Material, the updated surface chemistry set has been attached, as well as a brief description of the five fundamental mechanisms in SiO_2 etching on which it is based.

The reactor scheme and standard operating conditions in HPEM are based on the experimental settings of the Leybold F2 reactor, as discussed in Section 2.1 (see Figure 2 and Table I). Contrary to our previous investigation [33] and to the experiments, CF_4/Ar at a ratio of 10/90 was used as default for the inlet gas, instead of CHF_3/Ar at a ratio of 25/75, for four reasons: (i) the former mixture does not contain hydrogen, which reduces the number of assumptions and uncertainties in the gas and surface chemistry sets, (ii) the former mixture generally provided more stable simulations with MCFPM, (iii) the main etching mechanisms in both mixtures are very similar, in particular with regard to the neutral transport, and (iv) the gas ratio of 10/90 lies closer to the operating conditions used in many industrial plasma etching setups with fluorocarbon plasmas. In other words, CF_4/Ar at a ratio of 10/90 may be considered representative for the experimental conditions on a qualitative level. This permits to investigate trends in ARDE as a function of the parameters further discussed in Section 3, with a qualitative interpretation of the result that applies to the experiments as well. For comparison, we also performed a few simulations with the same settings as in the experiments.

Table II lists the standard settings of MCFPM for the parameters that were adjusted during the study. The meaning of each parameter will be clarified in the corresponding sections of this manuscript. The initial

profile of the hardmask for some of the used CD values is shown in Figure 3, based on the experimental initial profiles. Note that the experiment-based initial SoC hardmask profile displays a mushroom shape for CD = 36 nm, due to the processes during the preceding pattern transfer steps, as discussed in more detail in Refs. [36, 37]. Moreover, the initial etch mask sidewall angle for CD = 72 nm is taken 0° in the simulations, to approximate the experimental profile. For all wider features, the initial etch mask sidewall angle was found to be α = 8° in the experiments to a good approximation, and was therefore kept constant at this value in the simulations. The experiment-based profiles were, however, not made exactly identical to the initial profiles observed in the experiments, e.g. with regard to the rounded edges, partly to permit a straightforward interpretation of the results. We do not expect these deviations to affect the simulation results a lot, as indicated by our preliminary computational study. Simulations were performed in series for CD values of 36, 72, 100, 133, 167, 200, 300 and 600, optionally extended with 1000 nm. This included two additional simulations for CD = 36 and 72 nm with a hardmask sidewall angle of 8° and without mushroom shape, in order to assess the effect of the shape variation. For each simulation series, the etching result was investigated at an etch depth around 110-130 nm. The exact etch depth was obtained from the corresponding etched profile, by averaging the trench bottom depth over five subsequently equidistant locations, i.e. at the sides and center of the trench, and two points in between them. This data extraction method was found to be sufficiently accurate for the purpose of the present work, as demonstrated by the error analysis discussed in Appendices B and C. Dividing the calculated etch depth by the associated etch time provided the etch rate as a function of the CD.

Table II. Standard settings of the MCFPM simulations in this work.

Parameter	**Value**
Initial etch mask sidewall angle α	8°
Exponential factor λ *for diffusive desorption*	1
Maximal angle θ_{max} *for diffusive desorption*	90°
Incident F flux ($cm^{-2}s^{-1}$)	2.1×10^{17}
Incident CF_4 *flux* ($cm^{-2}s^{-1}$)	9.7×10^{16}
Incident flux of other neutrals ($cm^{-2}s^{-1}$)	2.9×10^{16}
Incident Ar^+ *flux* ($cm^{-2}s^{-1}$)	2.7×10^{15}
Incident flux of other ions ($cm^{-2}s^{-1}$)	1.5×10^{15}
Average ion energy (eV)	314

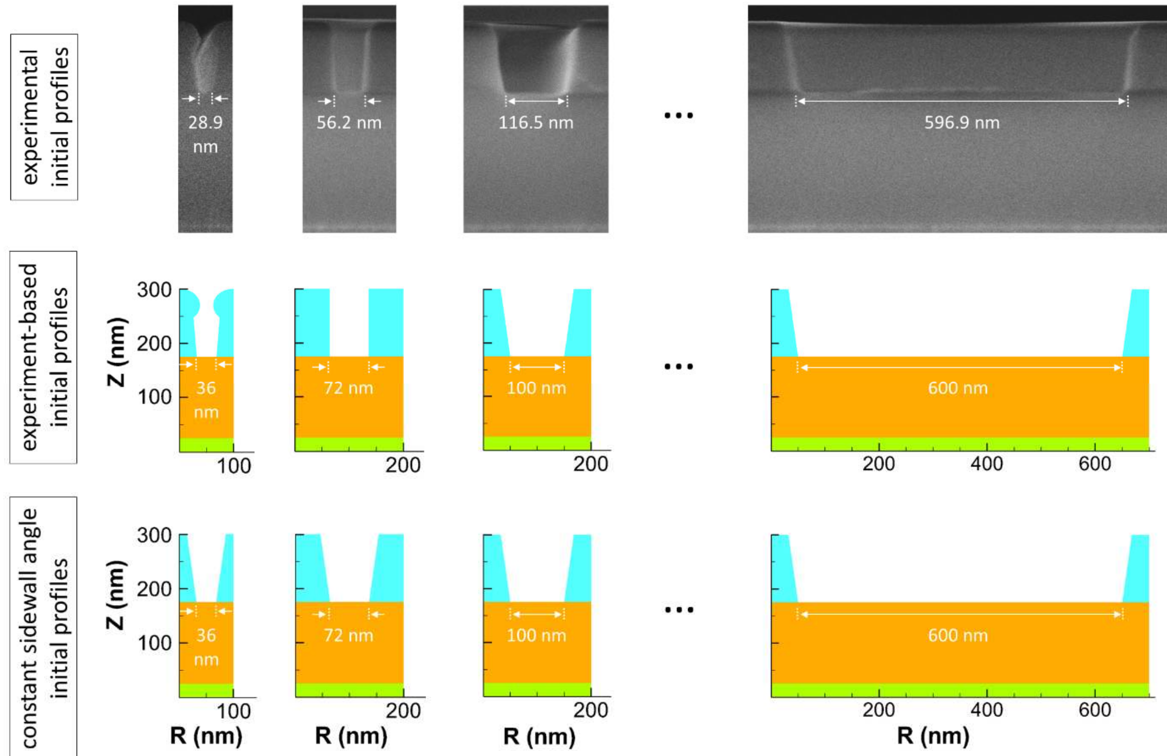

Figure 3. Initial etch mask profiles (top) as observed in the experiments, (middle) as used in the simulations for the experiment-based series, and (bottom) as used in the simulations for the more ideal series with a constant hardmask sidewall angle of α = 8°. The two simulation series only differ for CD = 36 and 72 nm, where the etch mask displays a mushroom shape and a sidewall angle of 0° in the experiment-based case, respectively. Note the TiN stop layer at the bottom of the SEM images, corresponding to the light green stop layer in the simulations. The thickness of the SiO_2 layer (in orange) was chosen smaller in the simulations (150 nm) than in the experiments (242.1 nm), to reduce the computational time. On the other hand, the initial thickness of the SoC hardmask (in light blue) was equal in the experiments and simulations.

3. Results and discussion: identifying the neutral transport mechanisms underlying ARDE

3.1 Shadowing and the diffuse reflection mechanism for neutrals in ARDE

The empirical ARDE curves obtained with the Leybold F2 reactor are shown in the top panel of Figure 4. A local maximum in the etch rate is consistently observed around a CD of 70 to 150 nm, i.e. an aspect ratio of about 0.5 to 1.4. Although this maximum has not received much attention yet in past research on ARDE, a transition from an inverse RIE lag at low aspect ratios to a regular one at high aspect ratios has been reported on a few occasions. In most cases, however, the inflection point is located at a higher aspect ratio. Doemling et al., for instance, observed a maximal etch rate at an aspect ratio around 9.4 for SiO_2 etching with CHF_3 in an ICP reactor [8]. Kokkoris et al. were able to approximately reproduce the

corresponding ARDE curve by means of a model of SiO_2 etching with a generic fluorocarbon plasma [15]. Accordingly, they attributed the inverse RIE lag portion of the curve to an increasing surface fraction of naked substrate material and thus an increasing physical sputtering yield as a function of the aspect ratio. The same model also predicted local maxima at aspect ratios ranging from 6 to 12 for other process conditions. Similarly, Kushner and co-workers observed a temporary increase of the instantaneous etch rate in their 3D MCFPM simulations of Si etching with Ar/Cl_2 plasmas at an aspect ratio of about 6 [7]. This peak emerged when the incident neutral-to-ion flux ratio was increased, the radical chlorine recombination probability on the sidewalls was decreased or the incident neutral angular distribution was tapered. In a more recent study with 3D MCFPM on SiO_2 etching with $Ar/C_4F_8/O_2$ mixtures, the instantaneous etch rate displayed an inflection point at an aspect ratio around 4, which was attributed to ion funneling [38].

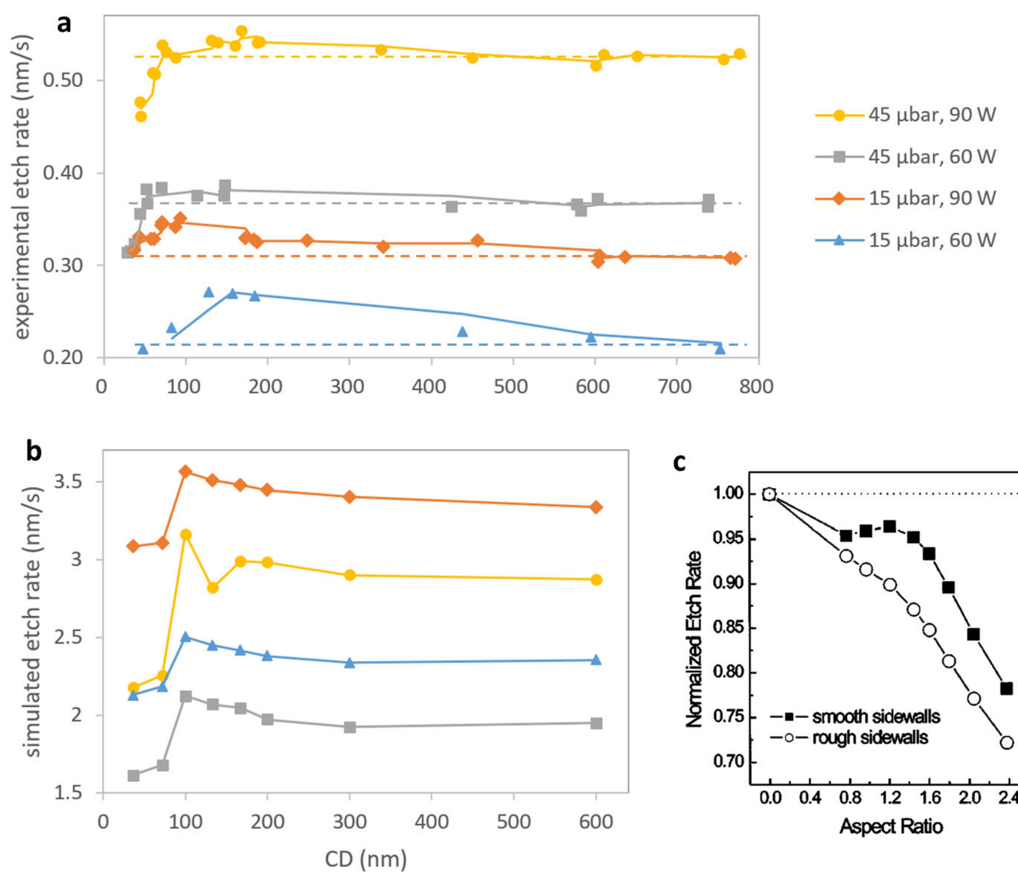

Figure 4. (a) Experimental and (b) simulated ARDE curves for identical conditions at a gas ratio of CHF_3/Ar = 15/45. The full lines represent the 2-period moving average for the experimental data series and linear interpolation for the simulated series, to guide the eye. The horizontal dashed line on each experimental curve serves as a reference relative to the local maximum, indicating the etch rate at the highest CD values. As an exception, the experimental data for 15 µbar and 60 W has been obtained from only one sample instead of two, with most data points based on one or two SEM images instead of three or more, so the corresponding ARDE curve is less reliable in comparison to the other ones. For the simulated curves,

only the experiment-based initial etch mask profiles have been used. (c) Normalized etch rates measured by Hwang et al. at the bottom center of millimeter-sized trenches under a CF_4 plasma chemistry as a function of the aspect ratio. (c) Reprinted with permission from [19]. Copyright 2004, American Vacuum Society.

Schaepkens et al. found the inflection point in ARDE around 3.4 to 5.1 in their SiO_2 etching experiments with CHF_3 ICP [14]. Yunkin et al. obtained an even lower empirical value of 3 for Si etching with $SF_6/C_2Cl_3F_3$ CCP [32]. They qualitatively reproduced the corresponding ARDE curve by means of a Monte Carlo model, with the local maximum at an aspect ratio of 1.7. Based on this agreement, they explained the inverse RIE lag with ion scattering from the sidewalls, which caused microtrenches at the bottom edges for wide features. By decreasing the CD, the microtrenches would merge, resulting in a higher etch rate. A similar conclusion was made by Hwang et al., who investigated ARDE for millimeter-sized SiO_2 trenches under a CF_4 chemistry in a transformer-coupled plasma etcher [19]. They compared the etch rate for two sidewall roughness conditions: one with a smooth thermally grown surface and the other with a polishing-induced root-mean-squared roughness of over 30 nm (see Figure 4(c)). The smooth surface resulted in a local maximum of the etch rate at an aspect ratio of 1.3, which vanished for the rough surface. The authors therefore also concluded the maximum to originate from ion-scattering at the sidewalls and the merging of the resulting microtrenches. The same hypothesis was adopted by Tsuda et al., who found an inflection point at an aspect ratio of 3.6, using a Si etching model for a Cl_2 plasma containing atomic oxygen [16]. According to their interpretation, passivation of the trench bottom by the O radicals (see Section 1) formed a subordinate mechanism in the inverse RIE lag. However, as we will demonstrate below, these observations can also be explained by means of an alternative mechanism based on the diffuse reflection of neutrals, which has received less attention up to now.

A local maximum in the etch rate was also observed in other chemistries, at an aspect ratio around 1 for Al etching with a $BCl_3/Cl_2/N_2$ plasma chemistry [31], around 4 for InP etching with Cl_2 ICP [30] and at 3.0 for $Al_{0.8}Ga_{0.2}As$ etching with $Cl_2/BCl_3/CH_4$ ICP [18]. More dedicated and accurate experiments are desirable to fully substantiate the local maximum and its features, such as the exact CD and aspect ratio at which it appears, its magnitude, and how these parameters vary with the experimental settings. In the remainder of the present work, however, we take a different approach, by investigating its origin by means of multiscale modeling.

The multiscale model indeed confirms the local maximum in the etch rate around a CD of 100 nm, i.e. an aspect ratio of about 1.2, as shown in Figure 4(b). It, however, overestimates the average etch rates for the experimental conditions, because we did not empirically benchmark it with a top-down approach, in order to keep the number of assumptions in the surface chemistry set to a minimum (see Section 2.2). An in-depth discussion on the possible causes of this deviation can be found in our previous work [33]. Regarding the ratios between the average etch rates, similarities as well as discrepancies are observed. As demonstrated in Table III, the simulations predict a ratio of 1.44 between the average etch rates ER_{90W} at a power of 90 W and ER_{60W} at 60 W, in satisfactory agreement with the experiments. On the other hand, the ratio between the rates $ER_{45\mu bar}$ at a pressure of 45 µbar and $ER_{15\mu bar}$ at 15 µbar is underestimated with a factor of about 1.9. This can partly be explained with the thickness of the deposited polymeric layer at the trench bottom, which is not implemented in the model, as we have kept the surface processes limited

to a lean chemistry for now. Inaccuracies in the calculated incident fluxes or ion energies may also contribute to this deviation, because the gas chemistry set in HPEM has not been meticulously benchmarked for the used conditions. Nonetheless, the observed deviation does not restrict our investigation in the remainder of the present work, as we will focus on the ARDE trend instead of the absolute etch rate values or the pressure effect.

Table III. Experimental and simulated average etch rate ratios ER_{90W}/ER_{60W} between the power settings of 90 W and 60 W, and $ER_{45μbar}/ER_{15μbar}$ between the pressure settings of 45 µbar and 15 µbar, for otherwise identical conditions.

	ER_{90W}/ER_{60W}		$ER_{45μbar}/ER_{15μbar}$	
	15 µbar	**45 µbar**	**60 W**	**90 W**
Experiment	1.36	1.45	1.51	1.61
Simulation	1.44	1.44	0.82	0.82

Note that several aspects of the deposited polymer layer are taken into account in the simulations. For instance, a polymer layer leads to passivation of the sidewalls [39] and can therefore reduce etch byproduct redeposition on the surface of the etched structure. This is in line with the molecular dynamics simulations by Tinck et al. [40], which have been used in the design of the surface chemistry set. Also the local chemistry of the polymer layer is included in the set, by differentiating between the $CF_{x\ (s)}$ and $SiO_2CF_{x\ (s)}$ surface groups for x values ranging from 0 till 4.

On the other hand, the main aspect of the polymer layer that the model does not consider is its thickness. For a layer on the etch front of high aspect ratio microstructures, the thickness can contribute to aspect ratio dependent etching in the vertical direction [41]. Nonetheless, for low aspect ratio features, this thickness is not expected to have a significant effect on ARDE. Next to that, the polymer layer may also either positively or negatively affect the etched surface roughness, depending on the etch conditions [42, 43]. For our simulations, this function is not required, because the etched surface remains sufficiently smooth. Additionally, the polymer layer may affect the charging effects and therefore the charge-related contribution to ARDE, for instance by a high electrical conductivity of the deposited polymer [44-46]. Yet, the influence of charging on ARDE is expected to be small for the low aspect ratios considered in our investigation. Therefore, the absence of charging and the polymer layer thickness in our simulations is expected to cause only a small deviation in the shape of the ARDE curves.

More precisely, the absence of the polymer layer thickness in the surface chemistry set is intentional, in order to keep the model as transparent as possible. The individual reaction probabilities of the incident ions with the different surface groups are namely not known as a function of these aspects of the polymer layer. Due to this gap in the fundamental data, these aspects can only be implemented in the surface chemistry set from a top-down approach, which would bring with it several new assumptions and uncertainties in the set. As discussed in our previous work [33], the number of assumptions in the set is therefore kept to a minimum. Instead, all surface reactions are based on elementary data found in the literature, e.g. from molecular dynamics simulations or ion-beam experiments. This allows the set to be

used for a fundamental study like the one that we will perform in the remainder of the present paper. Even so, we plan to include the polymer layer thickness in the surface chemistry set for future studies, in order to investigate its effect.

As a side note, the temperature effect on ARDE due to thermal polymer etching or a shift in sticking coefficients of the neutrals is expected to be small for the considered aspect ratio range in our study. The heat is namely supplied to the surface by the ions, for which the effect on ARDE by shadowing and charging is expected to be less dominant in the considered range as compared to the neutrals. As such, the heat supply to the etched surface should be fairly constant as a function of the aspect ratio in our experiments. The surface temperature can, however, affect the overall magnitude of the etch rate, causing a vertical shift of the experimental ARDE curves in Figure 4. This shift may contribute to the observed shifts relative to the simulated curves, but is unlikely large enough to be a dominant contributor. This lies in line with the well predicted input power effect by the model, which is closely related to the heat supply by the plasma on the surface.

To summarize the discussion on Figure 4, the agreement between the simulated and measured ARDE curves is mostly qualitative, but also partly quantitative in the following aspects:

1. The model accurately describes the input power effect, as shown in Table III.
2. Excluding the experiment at 60 W and 15 µbar for reasons discussed in the caption of Figure 4, the local maximum in the etch rate lies in the aspect ratio range from 1.0 to 1.4, consistent with the value of 1.2 predicted by the model.
3. Excluding the same experiment, the drop in etch rate from the local maximum to the largest CD values in Figure 4 is also described in a satisfactory way by the simulated ARDE curves, both in shape and magnitude.

In order to track down the origin of the local maximum in the etch rate, we note that the ARDE curve can be understood as the superposition of a monotonously increasing component (i.e. normal RIE lag) and a monotonously decreasing component (i.e. inverse RIE lag). We therefore propose the hypothesis that ARDE in MCFPM results from two underlying mechanisms, each corresponding to one of these components. The normal RIE lag component can most straightforwardly be explained with the shadowing effect for incident ions and neutrals combined, as will be demonstrated in Section 3.2. This effect namely implies a reduction of both the ion and neutral fluxes arriving at the etched trench bottom as the aspect ratio of the feature becomes larger, i.e. for smaller CD. The dominant etching mechanism consists of ion-assisted chemical etching, by physisorption of fluorocarbon gas particles, such as CF_4 or CHF_3, and subsequent bombardment of the surface with inert ions, such as Ar^+. Both these neutrals and ions have an overall etching function, despite the initial deposition of the neutrals. Therefore, a reduction of their flux at the bottom of a trench will reduce the etch rate.

Yet, shadowing alone cannot be responsible for the local maximum in the ARDE curve. Even when other incident plasma species with a less dominant role are taken into account, their flux will scale in a similar way as CF_4 or Ar^+, depending on whether they are cold neutrals, or kinetic ions and hot neutrals, respectively. The second, inverse RIE lag component of the ARDE curve therefore has a different origin.

According to our hypothesis, it is due to the re-emission of neutral species from the sidewalls of the hardmask and etched trench. Molecular species such as CF_4 namely first get physisorbed at the sidewalls, exchange thermal energy with the surface and accordingly get re-emitted in a thermal manner. This thermal re-emission ideally occurs according to Knudsen's cosine law, analogous to Lambert's cosine law for light (see Figure 5(a)), corresponding to so-called diffuse reflection, as well-established from vacuum studies [47-49]. MCFPM takes into account this process, by stochastically releasing each neutral species after a surface interaction, which can be either physical or chemical in nature, in a modifiable Lambertian distribution along the surface normal, as further explained in Section 3.2. Due to the axisymmetric shape of this distribution, roughly half of the re-emitted species are released upward and the other half downward. For large CD values, the sidewalls are far apart and the downward fraction will almost entirely reach the trench bottom. When the sidewalls approach each other for decreasing CD, the downward flux of re-emitted species will first increase due to the overlapping contributions of both sidewalls (see Figure 5(d)). This will cause more CF_4 to get physisorbed at the trench bottom, amplifying the etch rate and thus causing the inverse RIE lag for CD > 100 nm. Accordingly, the inverse RIE lag from the diffuse reflection of neutrals in combination with the regular RIE lag from the shadowing effect at smaller CD values explains the peak in the ARDE curves, as will be confirmed in Section 3.2. In Section 4.4, we will further show the etch mask profile to be decisive for the exact location of the etch rate maximum, according to our model. Deviations in this location between the experimental and simulated curves in Figure 4(a-b) can thus be partly attributed to uncertainties in the exact initial etch mask shape for the corresponding CD values.

In principle, however, the normal RIE lag for smaller CD values can also be explained with the diffuse reflection of neutrals alone, i.e. without the shadowing effect. Indeed, for decreasing CD, more and more of the downwardly emitted species will reach the opposing sidewall, where they once more have a chance of roughly 50% to be re-emitted upward. This counteraction of the downward flux is small for CD values several times larger than the etch depth. Yet, below a certain CD, it surpasses the amplifying effect, as illustrated in Figure 5(d). Accordingly, the total flux of these neutral species incident on the trench bottom declines as the CD becomes smaller, making the etch rate drop and thus causing a regular RIE lag. This can explain a local maximum in the ARDE curve in the case of a fixed initial etch mask sidewall angle, as observed in our simulations of Section 4.4. Still, this explanation seems less relevant for the experimental initial profiles, for which the shadowing effect has a much stronger influence on the etch rate, as will be shown in Section 3.2.

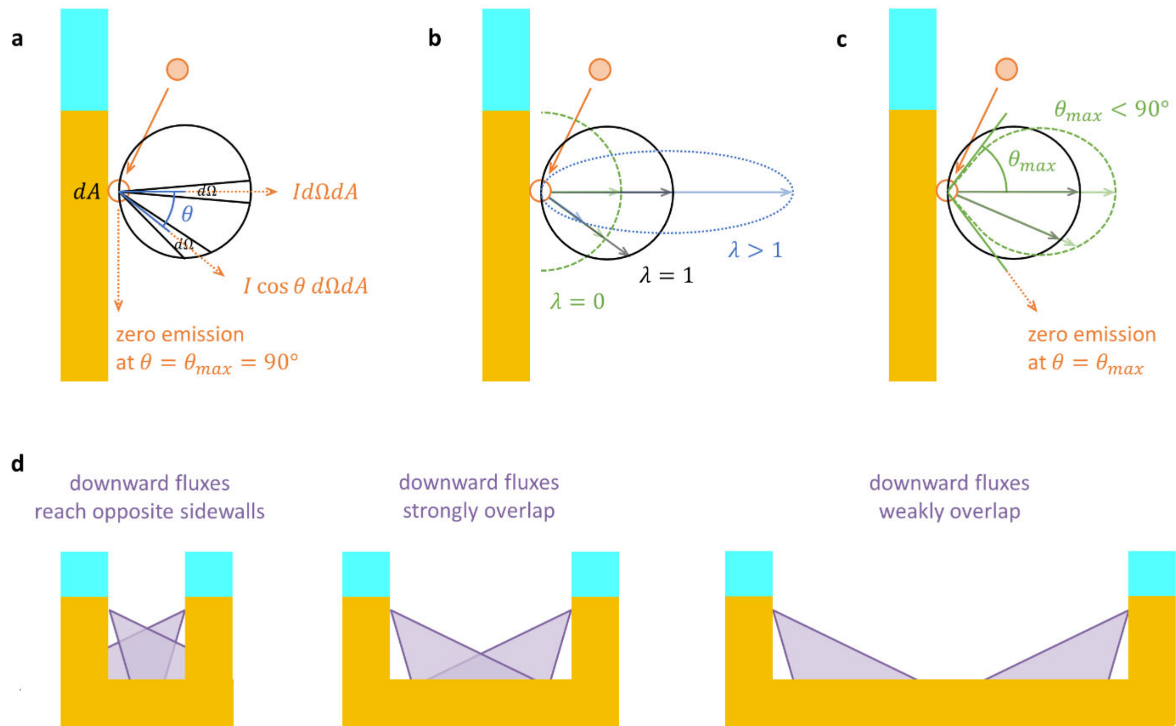

Figure 5. Schematic illustration of diffuse reflection. (a) The unmodified Knudsen's cosine law, where a neutral particle interacts with the surface and subsequently thermally desorbs under an angle θ with the surface normal according to the distribution $I \cos\theta \, d\Omega dA$, with I the intensity, $d\Omega$ the solid angle differential and dA the surface area differential. (b) and (c) Knudsen's cosine law modified with the exponential factor λ and the maximal emission angle θ_{max}, as implemented in MCFPM. (d) Cartoon of the overlapping downward neutral particle fluxes (in purple) emitted from the opposite sidewalls for three different values of the CD.

As should be noted, other mechanisms may also contribute to the local maximum in the ARDE curve. An inverse RIE lag for the CD > 100 nm can, for instance, be attributed to a plasma chemistry rich in polymerizing passivating neutrals (see Section 1). Additionally, a charging effect can restrict ions in effectively reaching the etch front at higher aspect ratios [4, 50], contributing to a regular RIE lag for CD < 100 nm. The simulations do not take these effects into account. The qualitative agreement with the experiments therefore does not conclusively indicate shadowing and diffuse reflection as the only underlying mechanisms. However, we aim to demonstrate with the present work how the ARDE curve shape can be explained in a self-consistent way by means of shadowing and diffuse reflection alone, i.e. without taking into account charging effects and the polymer layer thickness. Due to the universal nature of shadowing and Knudsen transport in plasma etching, this new insight is expected to be broadly valid in chemistries where ion-assisted chemical etching dominates.

In fact, our hypothesis should be considered as an alternative to, or an extension of, the ion funneling mechanism discussed above for an inverse RIE lag, where ion scattering at the sidewalls induces microtrenches that merge at high aspect ratios. An important question to be asked, though, is whether

any observed microtrenches are truly caused by ion-scattering. In both our experiments and our simulations, no well-defined sharp microtrenches appear, but the bottom instead displays a slight convex curvature with broadly rounded edges, as illustrated in Figure 6(a-b). Although ion scattering from the sidewalls may contribute to this effect, one would expect it to induce much sharper microtrenches. The diffuse reflection of neutrals on the sidewalls, on the other hand, forms a more plausible explanation for the observed bottom shape, as further verified in Section 3.2. As should be noted, our hypothesis applies to molecules as well as radicals, because the latter also undergo diffuse reflection, especially at passivated sidewalls. The importance of physisorption relative to chemisorption will be discussed in more detail in Section 4.2.

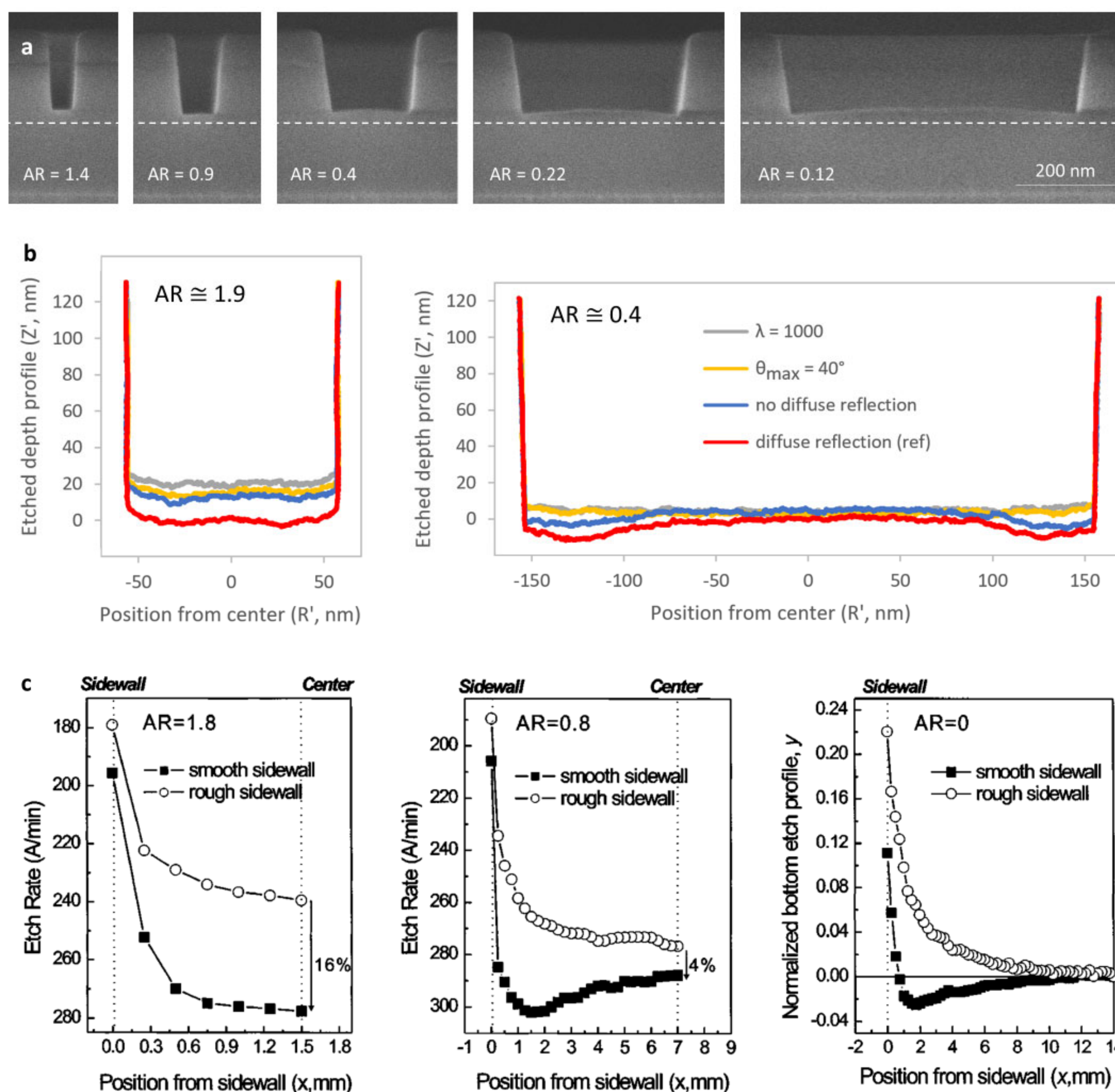

Figure 6. Etched profiles for different aspect ratios (AR), showing the rounded microtrenches in the trench bottom shape. (a) Experimental profiles for 15 µbar and 90 W, where the white dashed line serves as a reference for the vertical bottom position. (b) Simulated profiles at an etch time of 46 s for the standard

settings of Table II (red curve), compared with three cases further discussed in Section 3.2: without diffuse reflection of neutrals on the etch mask sidewalls, with an exponential factor $\lambda = 1000$ in the modified Lambertian distribution or with a maximum re-emission angle $\theta_{max} = 40°$ relative to the surface normal. (c) Experimental results obtained by Hwang et al. for millimeter-sized SiO_2 profiles under a CF_4 chemistry with smooth or rough sidewalls. (c) Reprinted with permission from [19]. Copyright 2004, American Vacuum Society.

Similarly, the aforementioned observations by Hwang et al. for smooth and rough sidewalls [19] also agree with our hypothesis. For smooth sidewalls and low aspect ratios, they namely measured an etched profile that resembles the one obtained in our MCFPM simulations with the standard settings (see Figure 6(b-c)). With rough sidewalls, the trench bottom became concave, in agreement with the profile changes in our simulations where the diffuse reflection of neutrals is eliminated or adjusted (see Section 3.2 and Figure 6). The rounded microtrenches that merge at higher aspect ratios therefore seem to originate from the diffuse reflection of neutrals, perhaps combined with ion scattering, rather than ion scattering alone. Our hypothesis is further supported by the simulation results by Kushner and co-workers in Ref. [7], where the temporary increase in the instantaneous etch rate generally did not exactly coincide with a delayed increase in the power density at the trench bottom due to incident energetic plasma species, i.e. ion funneling. Yet, the timing of the etch rate increase was also associated with an earlier temporary rise in Knudsen transport of Cl radicals toward the etch front, demonstrating that both ion funneling and neutral diffuse reflection were important.

Note that this agreement with the latter two studies illustrates the broad relevance of the diffuse reflection mechanism and therefore our investigation. Hwang et al., for instance, experimented with millimeter-sized features at a pressure of 6.7 μbar, which corresponds to a mean free path of the neutrals around 10 mm [19] (see also Appendix D). As long as the pressure is sufficiently low for the mean free path to be comparable or larger than the feature dimensions, the diffuse reflection mechanism needs to be taken into account due to its universal nature. It is also worth noting that the diffuse reflection mechanism relies more on aspect ratios than on absolute CD values in this sense. Accordingly, our hypothesis should also apply to features with smaller dimensions than the ones we considered, although stochastic effects may also play a role in such cases. Besides that, Kushner and co-workers considered plasma etching of fin field effect transistors (FinFETs) with CD values ranging from 33 to 67 nm for aspect ratios up to 14 [7]. While these aspect ratios significantly surpass the ones selected in our study, the Knudsen transport of the Cl radicals to the etch front was found to have a decisive effect. The diffuse reflection mechanism described in our hypothesis especially applies to the early etching stage of high aspect ratio microstructures, which affects the etch process at later stages. As such, our hypothesis remains relevant for a wide range of critical dimensions and aspect ratios, as well as various plasma chemistries.

However, experimentally verifying the diffuse reflection mechanism is a complicated task. Conventional plasma diagnostics namely only give direct information on the processes in the gas phase. Probing the plasma-surface interactions, on the other hand, requires advanced experimental setups, such as the ones described in the review by Allain and Shetty [51] and in the experimental study by Coumou et al. [52]. Even with such techniques, it would be very hard to obtain direct information on the diffuse reflection

mechanism and the shadowing effect. Therefore, we chose to verify our hypothesis by means of feature scale simulations, which forms the topic of Section 3.2.

3.2 Verifying the diffuse reflection mechanism

A first way to check the validity of our hypothesis on the local maximum origin is by eliminating the re-emission of neutrals at the sidewalls from the surface chemistry set, i.e. by assuming the incident neutrals to disappear after their interaction with a material cell. In order not to influence the surface chemistry too much, the neutral re-emission was only removed for the hardmask. Using the experiment-based initial etch mask profiles, the local maximum disappears this way as seen in Figure 7, and the rounded microtrenches at the lower aspect ratios become less pronounced as seen in Figure 6(b), confirming the hypothesis. When the etch mask sidewall angle is kept constant at α = 8° for CD = 36 and 72 nm, the ARDE curve is found to be monotonously decreasing at the standard settings (red line in Figure 7). Eliminating the diffuse reflection at the etch mask sidewalls once more leads to a monotonously increasing trend, but with a softer inclination. Therefore, the local maximum for the simulation series with the experiment-based initial hardmask profiles results from the combination of the shadowing effect and the diffuse reflection, further confirming the hypothesis.

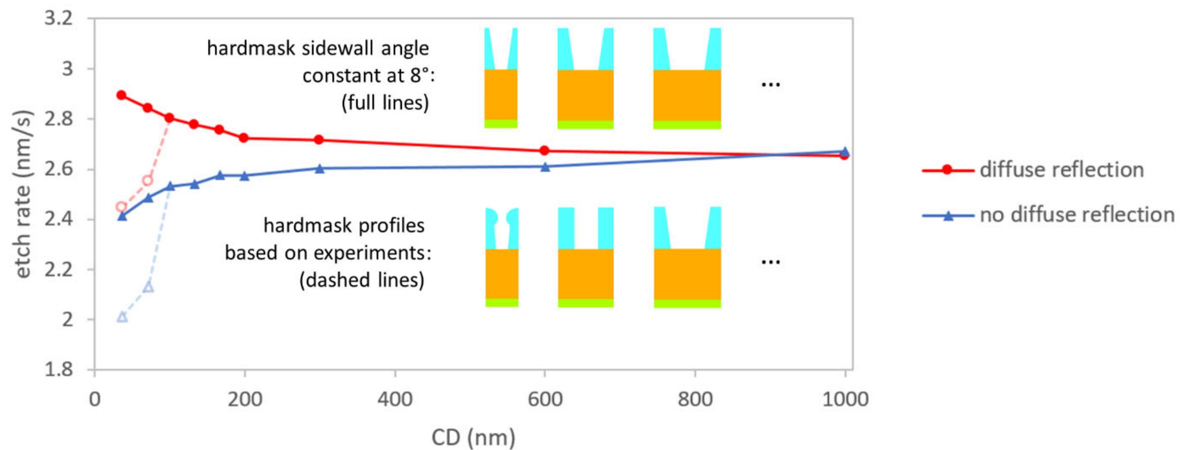

Figure 7. The simulated etch rate as a function of the CD, for neutral diffuse reflection from the etch mask enabled in the standard settings (red lines and circles) and compared with the situation where it is disabled (blue lines and triangles). Under the standard settings, all neutral species desorb from the etch mask surface immediately after interacting with it. When diffuse reflection at the hardmask is disabled, neutral species are assumed to be absorbed by its surface without changing the composition of the interacting surface group and without addition of a new surface group. The full and dashed lines serve as a guide to the eye. The full lines and the solid symbols indicate the simulation series with the constant initial hardmask sidewall angle, whereas the dashed lines and the hollow symbols show the series with the experiment-based initial profiles. Note that the two simulation series and thus the solid and dashed lines coincide for CD ≥ 100 nm, in agreement with Figure 3. Each curve is obtained from 5 simulation

series, as explained in Appendix B. For more details on the error analysis and the role of stochastics for these simulations series, see Appendix C.

In order to further verify our hypothesis on the local maximum origin, the diffuse reflection mechanism in the simulations can be modified. The most straightforward approach involves adjusting the Lambertian distribution in which the neutral species are re-emitted. In MCFPM, this is possible by means of two variable parameters: an exponential factor λ and the maximal angle θ_{max} that particles are permitted to be released with, relative to the surface normal vector (see Figure 5(b-c)). The standard settings in MCFPM use $\lambda = 1$ and $\theta_{max} = 90°$, corresponding to an ideal Lambertian distribution. The value $\lambda = 0$, in contrast, gives an isotropic emission and $\lambda > 1$ a distribution more peaked around the surface normal. The top panel of Figure 8 shows the effect of varying λ over different values. Isotropic desorption of neutrals from the sidewalls leads to a local maximum in the etch rate around CD = 167 nm, in agreement with the hypothesis. When the initial etch mask sidewall angle is kept fixed at α = 8° while reducing the CD to 72 and 36 nm, the etch rate rises again, likely due to more effective Knudsen transport of neutrals to the etch front. For the fixed initial etch mask sidewall angle series, increasing λ beyond 1 first seems to generate a peak in the etch rate around CD = 72 nm, to reverse the trend to a monotonously increasing one at and above a value of $\lambda = 4$. Simultaneously, the ARDE curve shifts down and the trench bottom becomes concave (see Figure 6(b)). This evolution is also in line with the hypothesis, because a more peaked neutral emission distribution along the surface normal corresponds to less effective Knudsen flow toward the etch front. Similarly, decreasing θ_{max} down to 40° reduces the Knudsen transport and therefore shifts the ARDE curve to lower etch rates, while reversing its trend to a monotonously increasing one at a fixed initial etch mask sidewall angle (lower panel of Figure 8). In addition, the rounded microtrenches disappear once more (see Figure 6(b)). This further confirms the hypothesis.

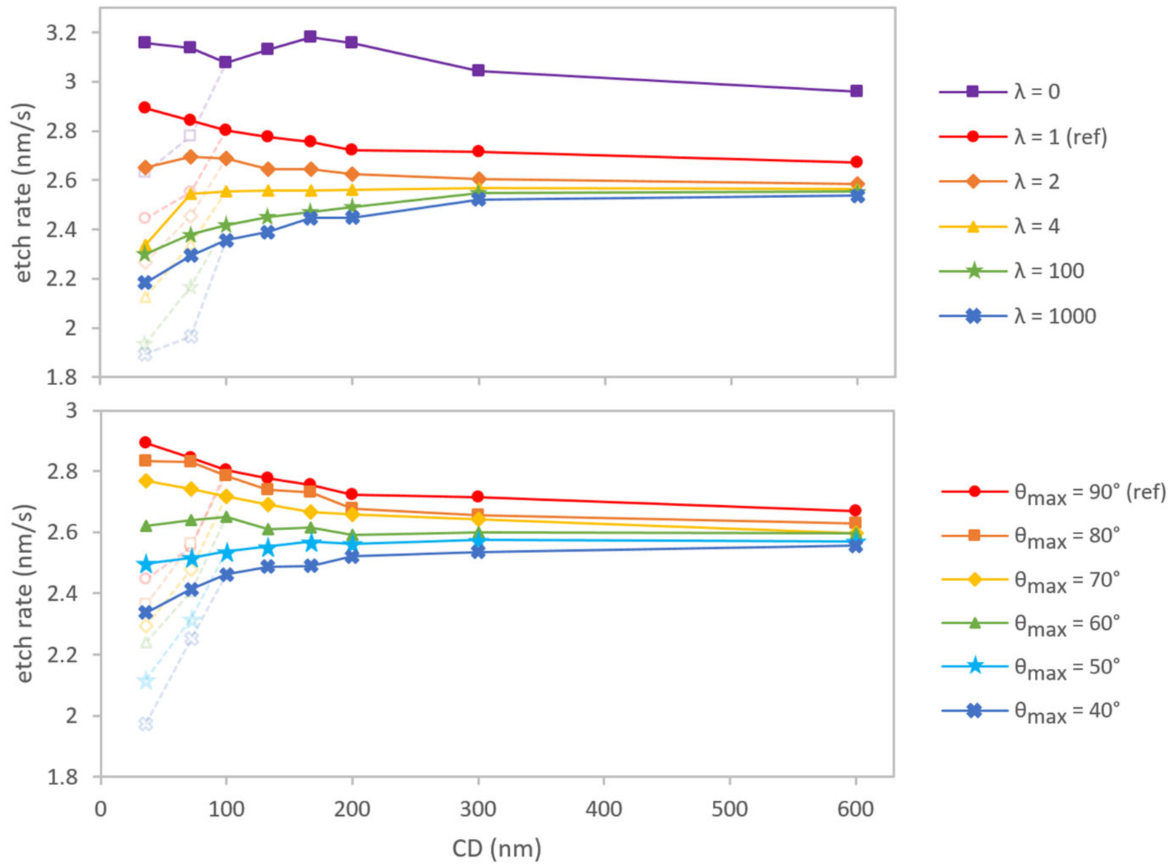

Figure 8. The simulated etch rate as a function of the CD for different angular distributions for thermal desorption of neutrals, (top) for different values of the exponential factor λ to modify the peakedness of the Lambertian distribution along the surface normal and (bottom) for different maximal emission angles θ_{max} relative to the surface normal. The full lines serve as a guide to the eye. The hollow symbols and dashed lines correspond to the experiment-based initial etch mask profiles and are depicted in low contrast for the ease of comparison.

For completeness, we also verified the minor influence of gas phase collisions on ARDE by means of the model, in line with the assumptions generally made in the scientific literature. This is discussed in more detail in Appendix D.

4. Results and discussion: parameters to regulate ARDE

4.1 Effect of the incident species fluxes

As discussed in Sections 2.2 and 3.1, the surface chemistry set allows a fundamental study of the etch process and ARDE in particular, because it is designed with a bottom-up approach. Such study is more complicated to be performed by means of experiments due to several reasons:

1. Parameters related to the incident plasma species, like the ion-to-neutral flux ratio and the ion energy and angular distribution, cannot be directly measured. Instead, they are estimated from plasma parameters obtained with plasma diagnostics, such as optical emission spectroscopy, mass spectrometry and Langmuir probes. This estimation is based on assumptions and mathematical models, which makes the measurement indirect.
2. With the exception of optical emission spectroscopy, these plasma diagnostics require specialized tools to be added in the reactor setup that may affect the processes in the reactor.
3. Changing the experimental parameters, such as the pressure, input power, gas flow rate and gas ratio, affects the plasma as a whole. Consequently, it is not possible to vary the incident flux ratios and ion energy and angular distribution in isolation of each other.

In contrast, the effect of the incident species, the surface chemistry and the initial etch mask profile can be studied in a straightforward manner with simulations. As such, we leverage this opportunity to investigate how these parameters may be used to regulate ARDE.

As discussed in Section 1, ARDE can be regulated and even reversed by adjusting the ion-to-neutral flux ratio in the presence of passivating species. Figure 9 presents the relative effect of the flux of CF_4, CF_x, F and F_2, as well as the ions, where each of these fluxes was independently varied from one another while keeping the other fluxes fixed. Lowering the flux with a factor of 0.2 beneath the reference conditions in the experiment-based etch mask profile series only has a significant effect for the ions, making the local maximum more expressed. For the fixed etch mask sidewall angle series, ARDE is reduced below CD = 100 nm when lowering the CF_4 flux to 20% of its value, but this improvement is undone when the experiment-based profiles are used. A five times higher flux, on the contrary, worsens ARDE significantly for CF_4, slightly for F and F_2, and not notably for CF_x radicals. Increasing the ion flux reduces ARDE in the fixed initial etch mask sidewall series, but makes it worse at CD < 100 nm for the experiment-based profiles.

Since CF_4 is the most prevalent neutral, this indeed confirms the ion-to-neutral flux ratio to be a decisive factor in ARDE. Increasing this ratio flattens the overall ARDE curve and reduces the local maximum. Because it can be regulated by means of experimental parameters, such as the pressure and input power, it offers a practical strategy for ARDE control. One should note, however, that changing these parameters will also influence the ion energy and angular distribution. Their effect on ARDE will therefore be discussed in Section 4.3.

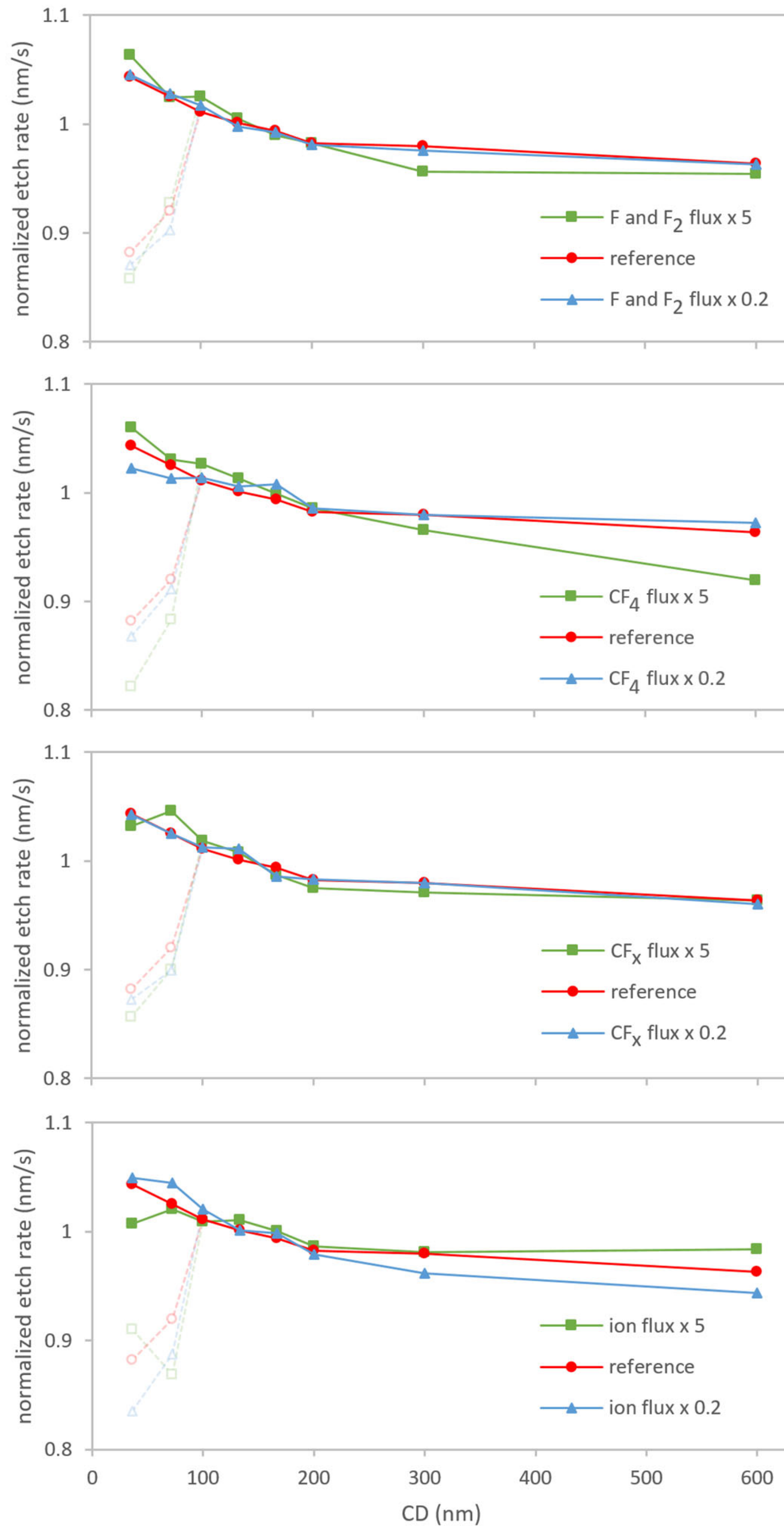

1.1
1
0.9
0.8
normalized etch rate (nm/s)
F and F_2 flux x 5
reference
F and F_2 flux x 0.2
CF_4 flux x 5
reference
CF_4 flux x 0.2
CF_x flux x 5
reference
CF_x flux x 0.2
ion flux x 5
reference
ion flux x 0.2
0
100
200
300
400
500
600
CD (nm)

Figure 9. The normalized etch rate as a function of the CD for variations in the flux of F and F_2, CF_4, CF_x radicals or ions with a factor of 5 or 0.2. Each curve is normalized to the average etch rate over the constant hardmask sidewall angle simulation series. The full lines serve as a guide to the eye. The hollow symbols and dashed lines correspond to the experiment-based initial hardmask profiles and are depicted in low contrast for the ease of comparison.

4.2 Effect of polymer deposition

In line with Section 1, another way to regulate and invert ARDE is by shifting towards a more polymerizing chemistry. The polymerizing nature of the fluorocarbon gas is currently not included in the surface chemistry set, as we consider a lean chemistry for the sake of simplicity (see also Section 3.1). There is namely still a lack of quantitative fundamental data on the deposited polymer layer thickness and composition as a function of the individual interactions between the plasma particles and the surface groups. Implementing it in the surface chemistry set in terms of the individual interactions would therefore include additional uncertainties, impeding the present fundamental study. Including its contribution into the simulations, however, will be required to further optimize the model. Although an accurate implementation of the polymerizing chemistry demands an in-depth study, the influence of additional CF_4 and CF_x deposition is easier to investigate. Figure 10 shows how the ARDE curve changes for such enhanced deposition. In agreement with the literature (see Section 1), the inverse RIE lag regime is amplified by the increased deposition when the initial etch mask sidewall angle is kept fixed. Unfortunately, the model fails to achieve a reasonable result for CD = 36 and 72 nm in the experiment-based series, due to unrealistically high polymer deposition during the first stage of the etching. This strong deposition results from ion shadowing by the mushroom-shaped etch mask at CD = 36 nm and the steep etch mask sidewall angle at CD = 72 nm (see Figure 3).

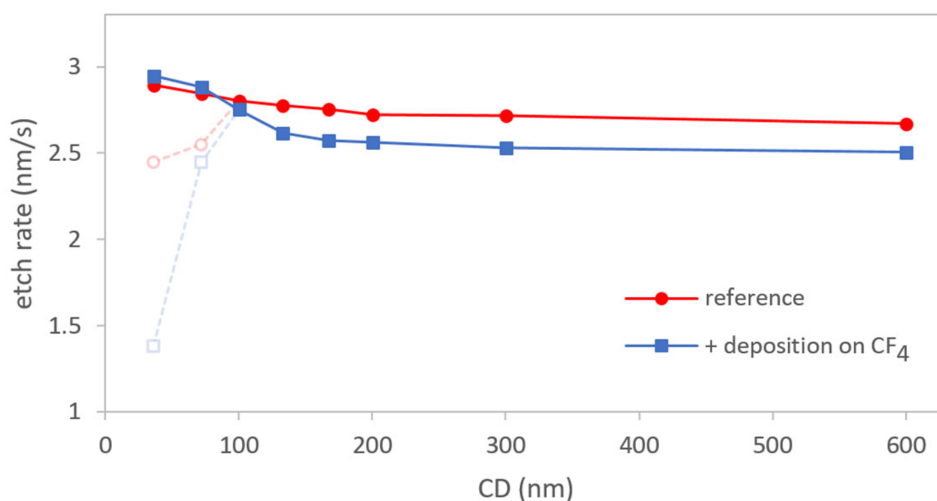

Figure 10. The etch rate as a function of the CD for enhanced CF_4 and CF_x deposition on $SiO_2CF_{4(s)}$ surface groups, in comparison to the reference settings. The full lines serve as a guide to the eye. The hollow

symbols and dashed lines correspond to the experiment-based initial etch mask profiles and are depicted in low contrast for the ease of comparison.

Note once more that the relative contribution of diffuse reflection versus polymerization to the inverse RIE lag at CD > 100 nm in the experimental ARDE curves is open for debate (see Section 3.1). Remarkably, this is closely related to the contemporary controversy on the importance of physisorption relative to chemisorption in ion-assisted chemical etching at room temperature [33, 53, 54]. According to an experimental atomic layer etching study by Sridhar, Ventzek and Ranjan, physisorption of hydrofluorocarbon gas precursors ($CH_xF_{(4-x)}$, x = 1-4) in the absence of a plasma suffices to modify a silicon nitride surface in a self-limiting manner, in order to remove it in the subsequent plasma-assisted desorption step [54]. Using first-principles calculations, Cheng and Hwang came to a similar conclusion for physisorption of CH_3F on Si_3N_4, because chemisorption did not yield a stoichiometrically reasonable pathway for the etching of a full atomic layer in their model [53]. We therefore conjecture that the same can be valid for SiO_2 etching with fluorocarbon-based plasmas or other plasma-surface chemistries. It is also worth noting that physisorption is considered a contributing mechanism in many atomic layer deposition processes and a major mechanism in cryogenic etching [55-58].

However, surface chemistry sets in the literature on plasma etching conventionally do not consider physisorption due to the long-hold and common belief that its role at room temperature is negligible in comparison to chemisorption. To the best of our knowledge, the bottom-up designed surface chemistry set used in our present simulations is the only exception to date, making it unique in its kind regarding this aspect as well. Because physisorption automatically precedes thermal desorption and thus also diffuse reflection, the prevalence of the latter depends on the prevalence of the former. The recent studies on the relevance of physisorption in ion-assisted chemical etching [53, 54] therefore also imply that diffuse reflection may very well play a more important role than originally assumed. Note in this regard that the surface chemistry set used in the present work includes chemisorption of CF_x radicals (and thus the resulting passivation of the surface), but predicts it to be subordinate to physisorption of CF_4 or CHF_3 under the investigated conditions. Due to its bottom-up design, this supports the relevance of physisorption relative to chemisorption on a fundamental level, as discussed in more detail in our previous work [33]. Although the corresponding physisorption probabilities are based on the desorption energies calculated in Ref. [40], they are estimated and therefore still prone to uncertainties. As such, more dedicated research is highly recommended to scrutinize the relative importance of physisorption in the plasma chemistry under consideration, as well as for chemistries in general.

In any case, even if chemisorption dominates over physisorption under specific conditions, the findings and discussion in the present work remain relevant. Radicals that do not react with the sidewalls namely also undergo diffuse reflection. Such interactions are expected to become prevalent when the sidewalls are significantly to fully passivated. This passivation reduces the sticking coefficients of the radicals, making their transport toward the etch front similar to the overall less reactive molecular species.

4.3 Effect of the ion energy and angular distribution

Because of the shadowing effect, the angular distribution width of the incident plasma species should also strongly affect ARDE. In practice, this parameter can only be changed significantly for the ions, by means of the bias voltage in an ICP reactor or the self-bias in a CCP reactor. Accordingly, its impact on the ARDE curve is shown in the top panel of Figure 11. Remarkably, a doubled ion angular distribution width does not aggravate ARDE, unless the experiment-based initial profiles are used. For a constant initial etch mask sidewall angle of α = 8°, halving the ion angular distribution width significantly reduces the difference in etch rate up to CD = 100 nm. Nonetheless, the etch uniformity worsens between CD = 100 and 200 nm. This may be due to a difference in etching of the sidewalls, but the exact cause is unclear for now. In practice, a narrowing of the ion angular distribution is achieved by accelerating the ions more in the plasma sheath. Correspondingly, the ion energy will increase, which may also have an effect on ARDE. Yet, the bottom panel of Figure 11 indicates that this effect remains very limited.

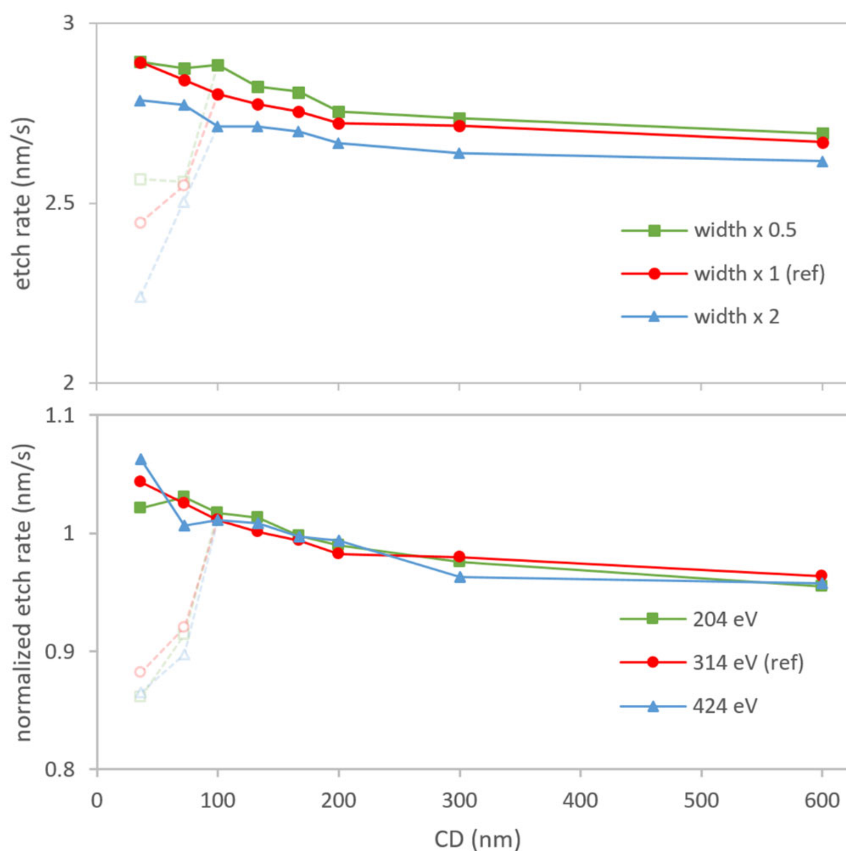

Figure 11. The etch rate and normalized etch rate as a function of the CD for (top) different ion angular distribution width and (bottom) ion energy. The full lines serve as a guide to the eye. The hollow symbols and dashed lines correspond to the experiment-based initial etch mask profiles and are depicted in low contrast for the ease of comparison.

4.4 Effect of the initial etch mask sidewall angle

Additionally, the shadowing effect and the diffuse reflection of neutrals will be influenced by the initial etch mask sidewall angle α. According to Figure 12, increasing α from 6° to 16° only has a moderate effect with an exception for CD = 36 nm. Decreasing it to 1°, on the other hand, results in a significant improvement of the etch uniformity. Note the local maximum at CD = 72 nm and CD = 100 nm for α = 2° and 1°, respectively, despite the constant hardmask shape. The diffuse reflection of neutrals can thus indeed lead to a peak in the ARDE curve by its own, without any additional shadowing, in agreement with our hypothesis in Section 3.1. For a hardmask sidewall angle of 0°, the local maximum becomes less pronounced, and the etch rate variation for critical dimensions below 100 nm is strongly amplified again. These results suggest α to be an effective parameter to regulate the extent of ARDE. To further optimize the etch uniformity, the above results suggest combining an initial etch mask sidewall angle of around α = 1° or 2° with a variation in other parameters, such as a narrower ion angular distribution and a fine-tuned ion-to-neutral flux ratio and polymerization. We plan an in-depth study on this topic in our future research. Next to that, we want to motivate researchers to consistently report the initial profile characteristics in any future ARDE study, such as the etch mask sidewall angle and any etch mask shape irregularities, because their influence on the final etch result should not be overlooked. For instance, as Figure 12 clearly illustrates, a smaller etch mask sidewall angle at high aspect ratios in comparison to low aspect ratios can determine the exact location of the inflection point between regular and inverse RIE lag. Note in this regard that the effect of the initial etch mask shape is a topic of high interest for advanced nodes as well (see e.g. Refs. [59-61]).

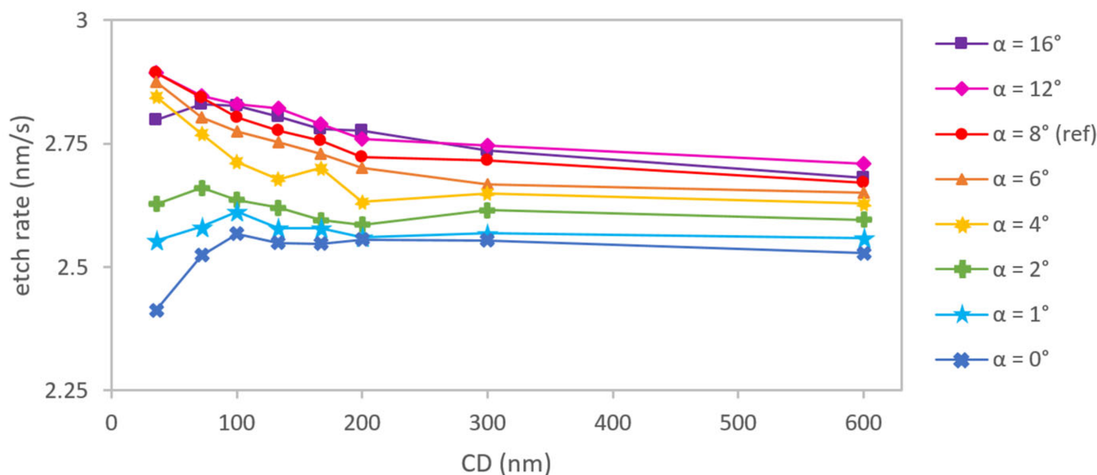

Figure 12. The etch rate as a function of the CD for different initial etch mask sidewall angles. The full lines serve as a guide to the eye.

5. Conclusion

In this work, we assessed the neutral transport mechanisms in ARDE by means of experiments and multiscale modeling of SiO_2 etching with a CHF_3/Ar or CF_4/Ar plasma. The experiments consistently reveal a local maximum in the etch rate around a CD of 70 to 150 nm. We were able to qualitatively reproduce

this maximum and the overall etch rate trend as a function of the CD using the Monte Carlo Feature Profile Model, for a lean chemistry in the absence of charging effects. As such, the observed trend can be explained with the combined effect of shadowing and diffuse reflection of neutrals, two mechanisms included in the model. To verify this hypothesis, the ARDE trend was investigated for the cases where diffuse reflection on the hardmask sidewall was only made possible for CF_4 or for no neutrals at all. In this way, our hypothesis has been confirmed and CF_4 was found to be the dominant species in the diffuse reflection mechanism. By varying the exponential factor λ and the maximal angle θ_{max} in the modifiable Lambertian distribution for diffusive desorption in the model, we further substantiated the role of diffuse reflection. Next to that, the ARDE trend for CD < 100 nm was shown to be strongly dependent on the etch mask shape, by comparing the influence of the experiment-based initial profiles and profiles with a fixed sidewall angle. This finding corroborates the role of the shadowing effect. Gas phase collisions, on the other hand, did not affect our simulation results, in line with the consensus in the literature.

The use of the bottom-up designed surface chemistry set in the multiscale model allows a further fundamental investigation of the ARDE trend. Each reaction in this set between a plasma species and a surface group is namely based on elementary data in the literature, obtained with dedicated experiments or first-principles simulations. We therefore additionally used the model to explore four methods to regulate ARDE: by varying the incident plasma species fluxes, the amount of polymer deposition, the ion energy and angular distribution and the initial hardmask sidewall angle. The CF_4 and ion fluxes, as well as the enhanced polymer deposition displayed a significant influence, in line with the insights from the literature. In contrast, the ion energy and angular distribution width only exhibited a mild effect. However, by far the strongest impact on ARDE was obtained with the etch mask sidewall angle, which therefore seems a critical control parameter.

6. Outlook

Based on our results, we want to motivate researchers to consistently characterize and report the hardmask shape and properties in any future ARDE studies. In fact, without such information, a detailed assessment of ARDE seems impossible. This involves both the geometry and material-dependent etch of the hardmask, as demonstrated by our simulations. For instance, the sticking coefficients of the reactive plasma species on the etch mask sidewalls can strongly affect their transport toward the etch front. In this regard, the relative importance of physisorption (i.e. low sticking coefficients) versus chemisorption (i.e. high sticking coefficients) deserves additional attention. A recent dedicated experimental study [54] and a first-principles investigation [53] of silicon nitride atomic layer etching with CHF_3 have demonstrated physisorption to be able to play a more essential role in ion-assisted chemical etching at room temperature than originally believed. The first-principles study even found chemisorption not to yield a stoichiometrically reasonable pathway. Because physisorption automatically precedes thermal desorption and thus diffuse reflection, it forms an essential process in the neutral transport mechanisms. The qualitative agreement between our experimental and simulation results in terms of the ARDE trend therefore indirectly supports the relevance of physisorption in plasma etching at room temperature. This support should be considered additional to the higher prevalence of CF_4 or CHF_3 physisorption relative to

CF_x radical chemisorption predicted by our bottom-up designed surface chemistry set, as reported already in our previous work [33]. However, extra research is required to further scrutinize the relative importance of physisorption versus chemisorption in various chemistries, as well as to identify the contribution of possibly competing mechanisms to the ARDE trend, such as charging effects or inverse RIE lag due to ion funneling or polymerizing species. Considering the trend toward increasingly smaller feature dimensions, quantum mechanical effects may additionally play a more important role than at larger length scales in the order of micrometers. A distinction between nanometer and micrometer length scales is therefore recommended when assessing each of these fundamental mechanisms. We accordingly want to motivate more dedicated experimental and computational investigations on these topics.

AUTHOR'S CONTRIBUTIONS

Patrick Vanraes: Conceptualization, Data curation, Formal analysis, Funding acquisition, Computational and literature investigation, Methodology, Validation, Visualization, Writing - original draft, Writing - review & editing. **Syam Parayil Venugopalan:** Conceptualization, Formal analysis, Theoretical and experimental investigation, Methodology, Project administration, Resources, Funding acquisition, Supervision, Validation, Writing - original draft, Writing - review & editing. **Matthieu Besemer:** Methodology, Writing - original draft, Writing - review & editing. **Annemie Bogaerts:** Funding acquisition, Project administration, Resources, Supervision, Writing - review & editing.

ACKNOWLEDGMENTS

P. Vanraes acknowledges funding by ASML for the project "Computational simulation of plasma etching of trench structures". P. Vanraes and A. Bogaerts want to express their gratitude to Mark J. Kushner (University of Michigan) for the sharing of the HPEM and MCFPM codes, and for the interesting exchange of views. P. Vanraes wishes to thank Violeta Georgieva and Stefan Tinck for the fruitful discussions on the HPEM code, Yu-Ru Zhang for an example of the CCP reactor code and Karel Venken for his technical help with the server maintenance and use. S.P. Venugopalan and M. Besemer wish to thank Luigi Scaccabarozzi, Sander Wuister, Coen Verschuren, Michael Kubis, Kuan-Ming Chen, Ruben Maas, Huaichen Zhang and Julien Mailfert (ASML) for the insightful discussions.

ROLE OF THE FUNDING SOURCE

This work was performed as a part of the project "Computational simulation of plasma etching of trench structures" funded by ASML, to investigate the physical principles of etch mechanisms and its impact on metrology marks.

DECLARATION OF COMPETING INTEREST

The authors declare the following financial interests/personal relationships which may be considered as potential competing interests: P. Vanraes is employed by the University of Antwerp, with funding by ASML for the project “Computational simulation of plasma etching of trench structures”. S.P. Venugopalan and M. Besemer are employed by the ASML research department working on “physical modeling of plasma etching”.

APPENDICES

Appendix A: Measurement of the experimental etch depth and etch rate

From the SEM images, the profile of the etched features was manually identified and approximated with linear sidewalls for the hardmask and the etched feature. The profile bottom was approximated with a horizontal line, the location of which was determined by having as much oxide material above it as below it along the intersection between the sidewalls, thus averaging the bottom shape. When a SEM image displayed an array of trenches, as usually the case for critical dimensions below 70 nm, the horizontal line was positioned on a height averaging the depth of the different trenches. Additional horizontal lines were drawn to more clearly visualize the top and bottom of the hardmask, as well as the three bright parallel interfaces found in the stop layer.

Finally, we analyzed the resulting SEM images containing the lines by means of WebPlotDigitizer (version 4.2), a publically available semi-automated image processing software developed by Ankit Rohatgi [34], in order to obtain the coordinates of the horizontal lines and their intersections with the linear sidewalls. The analysis method with WebPlotDigitizer was found to give an error below 1.0 nm for SEM images with a scale bar of 500 nm, down to 0.4 nm for a scale bar of 200 nm. In order to reduce the measurement error related to the manual positioning of the lines and the stochastic differences between SEM images, each profile was analyzed using a minimum of 3 images, and in some cases up to 12 images, particularly for lower critical dimensions, thus higher aspect ratios. For the determination of the etch depth, the distance of the profile bottom to the stop layer was subtracted from the distance between the stop layer and the etch mask bottom. The latter distance was obtained from the initial profiles before the etching process, averaged over 64 SEM images with 11 critical dimensions ranging from 30 to 600 nm. Due to the low contrast differences between the etch mask and the oxide layer, this distance was much harder to obtain from the profiles after etching, and was therefore only used to double-check the consistency of the measurements. Similarly, only the two upper interfacial lines of the stop layer were used to calculate the etch depth, whereas the lowest interfacial line was only used to double-check the measurements, due to its much lower contrast in the images.

Appendix B: Stochastics analysis method

As a kinetic Monte Carlo method, MCFPM uses a user-definable seed to initialize its pseudo-random number generator for particle release and collision probabilities. Varying this seed in otherwise identical simulations leads to different outcomes, while keeping it fixed results in identical output. Ideally, it should not significantly influence the overall simulation output, e.g. the etched profile, depth and rate, due to the high number of incident computational particles and their interactions. The pseudo-random character of the algorithm may, however, cause numerical artifacts and thus artificial errors in the simulation output. This forms a first motivation to carry out a statistical analysis of the simulation results, especially to quantify the computational error on the etch rate. Next to that, the etch rate calculation could be prone to errors in the post-processing of the simulation output, for instance by an inaccurate identification of the feature profile bottom or by insufficiently accounting for its surface roughness. By repeating a simulation with different seeds and post-processing its output with distinct data extraction methods, also this post-processing error can be quantified. Moreover, as we will discuss more thoroughly in Section 3.2, the stochastic nature of the underlying physical processes can also induce stochastics in the etch outcome, which thus has a physical origin. This brings forward a third motivation for such statistical analysis.

For these purposes, we repeated a few simulation series with four different seeds, thus providing five distinct simulation outcomes (including the one with the default seed) for otherwise identical settings. For each outcome, the etch depth was measured in two ways. The first method equals the procedure with the five subsequently equidistant points on the feature bottom, as described in Section 2.2 above. In the second method, the vertical coordinates of the mesh cells that constitute the feature profile bottom are extracted from the simulation output and averaged. The bottom edges are defined as the points where the sidewalls visually meet the lowest edge of the profile at a well-distinguishable angle, usually slightly greater than 90°, unless such angle cannot be specified or the edge lies below material cells, i.e. from the sidewalls or the etch mask. If such points cannot be determined, the edge is identified as the first point from the left or from the right that does not lie underneath material cells. We will refer to these procedures for the determination of the etch depth as the five points method (5PM) and the extraction method (EM), respectively. With each method, the etch depth and its standard error are accordingly calculated by means of five data points, each corresponding to another seed. As demonstrated in Appendix C, the five points method provides a sufficient accuracy to investigate ARDE by means of a single simulation series. It was consequently chosen as the standard post-processing approach, because it significantly reduced the analysis time in comparison to the extraction method.

Appendix C: Error and stochastics analysis

Figure C1 shows the results of the stochastic analysis for the ARDE curves in Figure 7, as performed with the method described in Appendix B. The following conclusions can be made:

- The error bars on the ARDE curves are sufficiently small to obtain a reliable ARDE curve with only one simulation series, instead of five series with different seeds (see also Appendix B).
- The extraction method is about twice as accurate as the five points method to calculate the etch rate for most data points, while for some data points it performs approximately the same. The

five points method, however, remains sufficiently accurate for the investigation purpose in the remainder of the present work. It was therefore selected as the default method, as it allows a faster analysis.

- For decreasing CD, the stochastic error in the etch rate starts to increase around CD = 200 nm, to roughly double at CD = 36 nm. This trend, however, seems independent of the diffuse reflection of neutrals at the etch mask.

The latter insight suggests that neutral diffuse reflection does not underlie or visibly amplify the stochastics. The standard error in the simulations may therefore have a purely computational origin. Nonetheless, such stochastic behavior can as well correspond to a physical effect. As seen in Figure C2, the etch depth and etched profile can vary significantly between neighboring features under certain conditions (e.g. 15 µbar and 90 W, as well as 45 µbar and 60 W or 90 W), while being fairly constant under others (e.g. 15 µbar and 60 W). The origin of this effect is unclear for now, requiring more dedicated research.

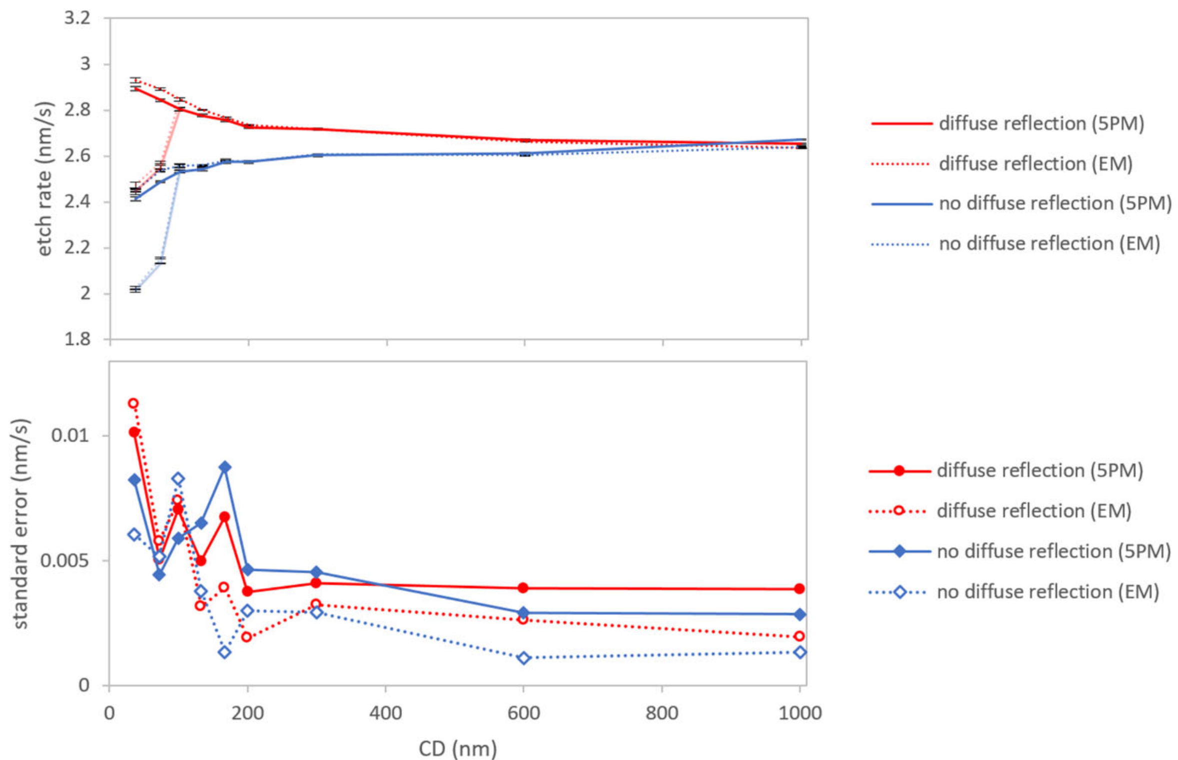

Figure C1. (top) The simulated etch rate and (bottom) its standard error as a function of the CD determined with the five points method (5PM) and extraction method (EM) for the two conditions in Figure 7 for the neutral diffuse reflection from the etch mask. The full and dotted lines serve as a guide to the eye. Whereas the top panel shows the simulation data for both the experiment-based and the constant sidewall angle initial profiles, the bottom panel only includes the latter for the sake of clarity.

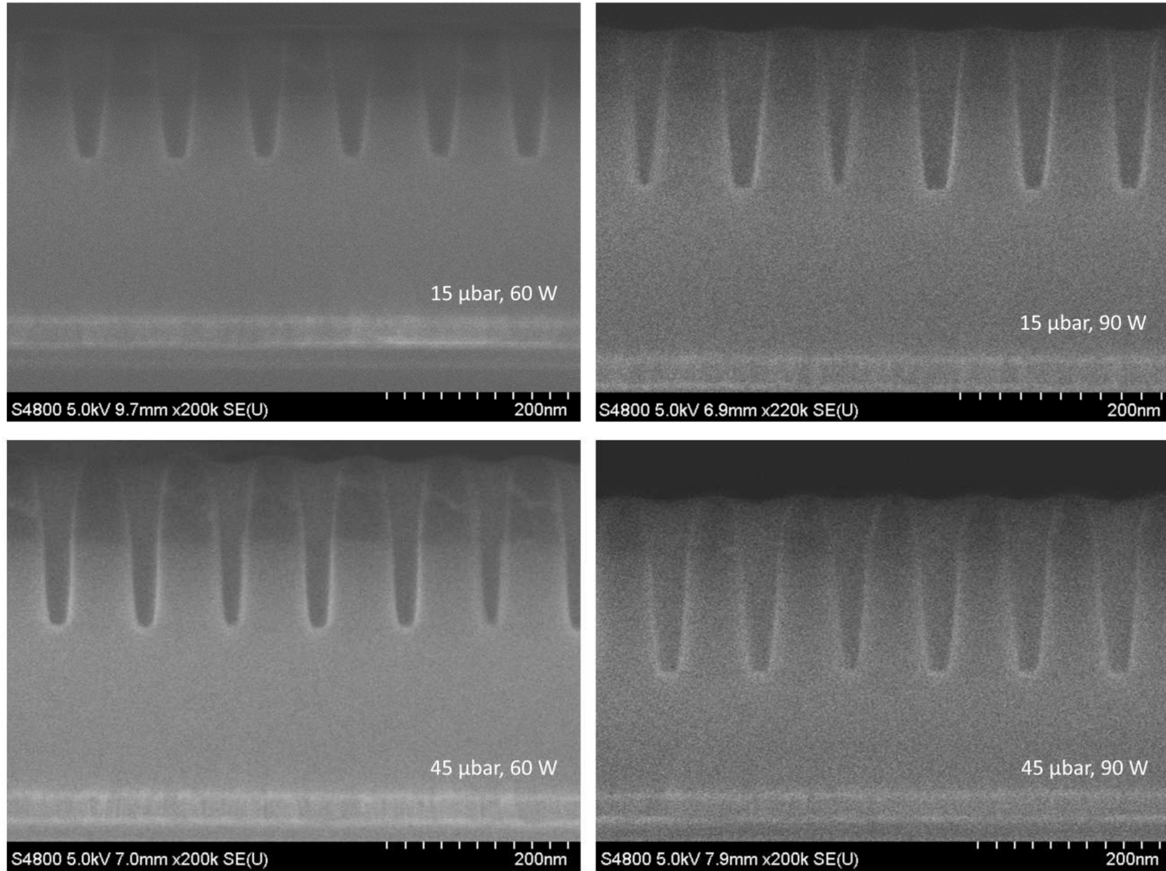

Figure C2. Stochastics in adjacent etched profiles observed under the four experimental conditions for CD values ranging around 28 to 39 nm.

Appendix D: Assessing the influence of gas phase collisions

Although diffusion in the gas phase is generally considered to have a minor influence at the feature scale due to the low pressure used in plasma etch reactors, it is still interesting to evaluate its effect on ARDE. In MCFPM, gas phase collisions can be included by defining a mean free path λ_{mfp} valid for all neutral species. The code accordingly attributes randomly chosen travel distances to the computational gas particles that average out to λ_{mfp}. After traveling such a distance without hitting a material cell first, a particle is assumed to scatter in an isotropic fashion with no loss in energy, representing a purely elastic collision. We estimated the mean free path from a hard sphere approximation using the formula [62]:

$$\lambda_{\mathrm{mfp}} = \frac{RT}{\sqrt{2}\pi d^2 N_A P}$$

Here, R is the gas constant, T the temperature, P the pressure, N_A the Avogadro constant, and d the diameter of the hard sphere approximating the particle shape. We selected CF_4 as the representative neutral particle in the gas phase, because of its dominant role in the surface chemistry. At the average

reactor pressure, an upper limit of λ_{mfp} = 4.34 mm was calculated from the C-F bond length of 132.3 pm [63], and a lower limit of λ_{mfp} = 1.03 mm including the C and F radii of 75 and 64 pm. In order to account for a possibly locally elevated pressure at the wafer surface due to the etch by-product efflux, also a 10 times lower value was considered. As shown in Figure D1, none of these values for λ_{mfp} provide a significant effect on ARDE, in line with the assumptions generally made in the scientific literature.

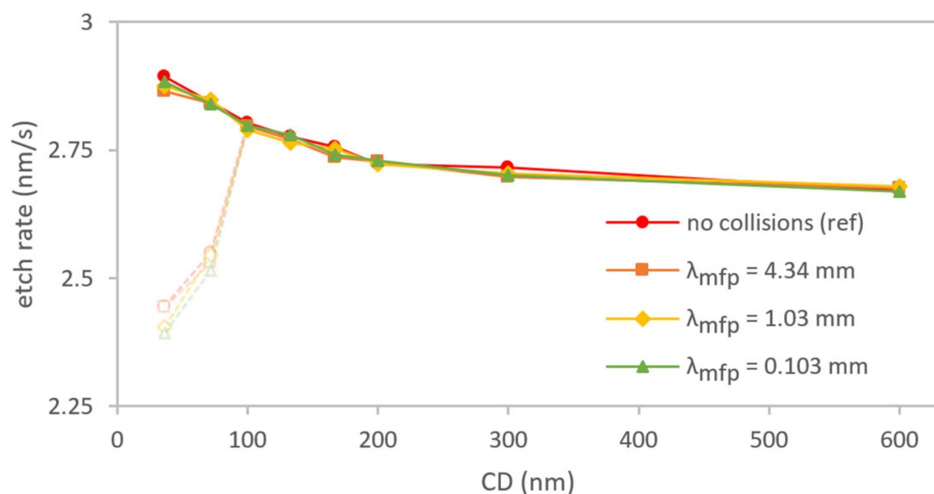

Figure D1. Simulated ARDE curves for different values of the mean free path λ_{mfp} as compared to the reference case without gas diffusion. The full lines serve as a guide to the eye. The hollow symbols and dashed lines correspond to the experiment-based initial etch mask profiles and are depicted in low contrast for the ease of comparison.

REFERENCES

1. Mulkens, J., et al. *Holistic approach for overlay and edge placement error to meet the 5nm technology node requirements*. in *Metrology, Inspection, and Process Control for Microlithography XXXII*. 2018. SPIE.
2. Jeong, J., et al. *Understanding advanced DRAM edge placement error budget and opportunities for control*. in *Metrology, Inspection, and Process Control for Microlithography XXXIV*. 2020. SPIE.
3. Džafić, H., M.R. Kamali, and S.P. Venugopalan, *Plasma sheath modelling to predict etch-induced overlay.* Journal of Physics D: Applied Physics, 2021. **55**(7): p. 075201.
4. Gottscho, R.A., C.W. Jurgensen, and D. Vitkavage, *Microscopic uniformity in plasma etching.* Journal of Vacuum Science & Technology B: Microelectronics and Nanometer Structures Processing, Measurement, and Phenomena, 1992. **10**(5): p. 2133-2147.
5. Chin, D., S.H. Dhong, and G.J. Long, *Structural effects on a submicron trench process.* Journal of the Electrochemical Society, 1985. **132**(7): p. 1705.
6. Ishikawa, K., et al., *Progress in nanoscale dry processes for fabrication of high-aspect-ratio features: How can we control critical dimension uniformity at the bottom?* Japanese Journal of Applied Physics, 2018. **57**(6S2): p. 06JA01.

7. Huard, C.M., et al., *Role of neutral transport in aspect ratio dependent plasma etching of three-dimensional features.* Journal of Vacuum Science & Technology A: Vacuum, Surfaces, and Films, 2017. **35**(5): p. 05C301.
8. Doemling, M., N. Rueger, and G. Oehrlein, *Observation of inverse reactive ion etching lag for silicon dioxide etching in inductively coupled plasmas.* Applied physics letters, 1996. **68**(1): p. 10-12.
9. Cheong, H., et al., *A study on reactive ion etching lag of a high aspect ratio contact hole in a magnetized inductively coupled plasma.* Plasma Sources Science and Technology, 2014. **23**(6): p. 065051.
10. Mori, M., et al., *Formation mechanisms of etched feature profiles during Si etching in Cl2/O2 plasmas.* Journal of Vacuum Science & Technology A: Vacuum, Surfaces, and Films, 2019. **37**(5): p. 051301.
11. Carlström, C., et al., *Cl 2⁄ O 2-inductively coupled plasma etching of deep hole-type photonic crystals in InP.* Journal of Vacuum Science & Technology B: Microelectronics and Nanometer Structures Processing, Measurement, and Phenomena, 2006. **24**(1): p. L6-L9.
12. Ono, K., H. Ohta, and K. Eriguchi, *Plasma–surface interactions for advanced plasma etching processes in nanoscale ULSI device fabrication: A numerical and experimental study.* Thin Solid Films, 2010. **518**(13): p. 3461-3468.
13. Knizikevičius, R., *Inverse RIE Lag during Silicon Etching in SF6+ O2 Plasma.* Acta Physica Polonica, A., 2020. **137**(3).
14. Schaepkens, M., G. Oehrlein, and J. Cook, *Effects of radio frequency bias frequency and radio frequency bias pulsing on SiO 2 feature etching in inductively coupled fluorocarbon plasmas.* Journal of Vacuum Science & Technology B: Microelectronics and Nanometer Structures Processing, Measurement, and Phenomena, 2000. **18**(2): p. 856-863.
15. Kokkoris, G., E. Gogolides, and A.G. Boudouvis, *Etching of SiO 2 features in fluorocarbon plasmas: Explanation and prediction of gas-phase-composition effects on aspect ratio dependent phenomena in trenches.* Journal of applied physics, 2002. **91**(5): p. 2697-2707.
16. Tsuda, H., et al., *Atomic-Scale Cellular Model and Profile Simulation of Si Etching: Analysis of Profile Anomalies and Microscopic Uniformity.* Japanese Journal of Applied Physics, 2010. **49**(8S1): p. 08JE01.
17. Knizikevičius, R., *Simulation of inverse reactive ion etching lag.* Vacuum, 2003. **72**(1): p. 53-57.
18. Mochizuki, M., et al., *Dry Etching of Al-Rich AlGaAs for Photonic Crystal Fabrication.* Japanese Journal of Applied Physics, 2011. **50**(4S): p. 04DG15.
19. Hwang, S.-W., et al., *Effect of sidewall roughness on the bottom etch properties of an SiO 2 trench produced in a CF 4 plasma.* Journal of Vacuum Science & Technology B: Microelectronics and Nanometer Structures Processing, Measurement, and Phenomena, 2004. **22**(4): p. 1953-1957.
20. Joubert, O., G. Oehrlein, and M. Surendra, *Fluorocarbon high density plasma. VI. Reactive ion etching lag model for contact hole silicon dioxide etching in an electron cyclotron resonance plasma.* Journal of Vacuum Science & Technology A: Vacuum, Surfaces, and Films, 1994. **12**(3): p. 665-670.
21. Westerheim, A., et al., *Substrate bias effects in high-aspect-ratio SiO2 contact etching using an inductively coupled plasma reactor.* Journal of Vacuum Science & Technology A: Vacuum, Surfaces, and Films, 1995. **13**(3): p. 853-858.
22. Adel, M., et al., *Optimized overlay metrology marks: theory and experiment.* IEEE Transactions on Semiconductor manufacturing, 2004. **17**(2): p. 166-179.
23. Radisic, D., et al. *Plasma etch selectivity study and material screening for self-aligned gate contact (SAGC)*. in *Advanced Etch Technology for Nanopatterning VIII*. 2019. SPIE.

24. Huard, C.M., et al., *Atomic layer etching of 3D structures in silicon: Self-limiting and nonideal reactions.* Journal of Vacuum Science & Technology A: Vacuum, Surfaces, and Films, 2017. **35**(3): p. 031306.
25. Panneerchelvam, P., et al. *Trilayer hard mark lithography and etch for BEOL manufacturing*. in *Metrology, Inspection, and Process Control XXXVI*. 2022. SPIE.
26. Raley, A., et al. *Outlook for high-NA EUV patterning: a holistic patterning approach to address upcoming challenges*. in *Advanced Etch Technology and Process Integration for Nanopatterning XI*. 2022. SPIE.
27. Ohara, J., et al., *Development of RIE-lag Reduction Technique for Si Deep Etching Using Double Protection Layer Method.* IEEJ transactions on electrical and electronic engineering, 2010. **5**(2): p. 125-130.
28. Kanarik, K.J., et al., *Overview of atomic layer etching in the semiconductor industry.* Journal of Vacuum Science & Technology A: Vacuum, Surfaces, and Films, 2015. **33**(2): p. 020802.
29. Biyikli, N. and A. Haider, *Atomic layer deposition: an enabling technology for the growth of functional nanoscale semiconductors.* Semiconductor Science and Technology, 2017. **32**(9): p. 093002.
30. Carlström, C., et al., *Comparative study of Cl 2, Cl 2∕O 2, and Cl 2∕N 2 inductively coupled plasma processes for etching of high-aspect-ratio photonic-crystal holes in InP.* Journal of Vacuum Science & Technology B: Microelectronics and Nanometer Structures Processing, Measurement, and Phenomena, 2008. **26**(5): p. 1675-1683.
31. Xie, R.J., J.D. Kava, and M. Siegel, *Aspect ratio dependent etching on metal etch: Modeling and experiment.* Journal of Vacuum Science & Technology A: Vacuum, Surfaces, and Films, 1996. **14**(3): p. 1067-1071.
32. Yunkin, V., et al., *Experimental study and computer simulation of aspect ratio dependent effects observed in silicon reactive ion etching.* Microelectronic engineering, 1996. **30**(1-4): p. 345-348.
33. Vanraes, P., S. Parayil Venugopalan, and A. Bogaerts, *Multiscale modeling of plasma–surface interaction—General picture and a case study of Si and SiO2 etching by fluorocarbon-based plasmas.* Applied Physics Reviews, 2021. **8**(4): p. 041305.
34. Rohatgi, A., *WebPlotDigitizer*. 2019: Pacifica, California, USA. p. https://automeris.io/WebPlotDigitizer.
35. Kushner, M.J., *Hybrid modelling of low temperature plasmas for fundamental investigations and equipment design.* Journal of Physics D: Applied Physics, 2009. **42**(19): p. 194013.
36. Koike, K., et al. *Optimize of shrink process with XY CD bias on hole pattern*. in *Advances in Patterning Materials and Processes XXXIV*. 2017. SPIE.
37. Ehara, K., et al. *Substrate damageless tri-layer process for advanced ArFi lithography*. in *Novel Patterning Technologies 2018*. 2018. SPIE.
38. Huang, S., et al., *Plasma etching of high aspect ratio features in SiO2 using Ar/C4F8/O2 mixtures: A computational investigation.* Journal of Vacuum Science & Technology A: Vacuum, Surfaces, and Films, 2019. **37**(3): p. 031304.
39. Zhang, D. and M.J. Kushner, *Investigations of surface reactions during C 2 F 6 plasma etching of SiO 2 with equipment and feature scale models.* Journal of Vacuum Science & Technology A: Vacuum, Surfaces, and Films, 2001. **19**(2): p. 524-538.
40. Tinck, S., E.C. Neyts, and A. Bogaerts, *Fluorine–Silicon Surface Reactions during Cryogenic and Near Room Temperature Etching.* The Journal of Physical Chemistry C, 2014. **118**(51): p. 30315-30324.
41. Nishikawa, K., et al., *Transport mechanisms of ions and neutrals in low-pressure, high-density plasma etching of high aspect ratio contact holes.* Thin Solid Films, 2000. **374**(2): p. 190-207.

42. Min, J.-H., et al., *Redeposition of etch products on sidewalls during SiO 2 etching in a fluorocarbon plasma. I. Effect of particle emission from the bottom surface in a CF 4 plasma.* Journal of Vacuum Science & Technology A: Vacuum, Surfaces, and Films, 2002. **20**(5): p. 1574-1581.
43. Wang, X., et al., *Scaling of atomic layer etching of SiO2 in fluorocarbon plasmas: Transient etching and surface roughness.* Journal of Vacuum Science & Technology A: Vacuum, Surfaces, and Films, 2021. **39**(3): p. 033003.
44. Donnelly, V.M. and A. Kornblit, *Plasma etching: Yesterday, today, and tomorrow.* Journal of Vacuum Science & Technology A: Vacuum, Surfaces, and Films, 2013. **31**(5): p. 050825.
45. Shimmura, T., et al., *Electrical conductivity of sidewall-deposited fluorocarbon polymer in SiO 2 etching processes.* Journal of Vacuum Science & Technology B: Microelectronics and Nanometer Structures Processing, Measurement, and Phenomena, 2002. **20**(6): p. 2346-2350.
46. Shimmura, T., et al., *Effects of fluorocarbon gas species on electrical conductivity and chemical structure of deposited polymer in SiO 2 etching processes.* Journal of Vacuum Science & Technology B: Microelectronics and Nanometer Structures Processing, Measurement, and Phenomena, 2004. **22**(2): p. 533-538.
47. Hurlbut, F.C. and R.J. Mansfield. *Calculated and Observed Pumping Speeds of a Shielded Cryogenic Pumping Surface*. 1963. Boston, MA: Springer US.
48. Füstöss, L., *Evaluation and calculation of gas flow through axially symmetric tubes.* Vacuum, 1983. **33**(1-2): p. 13-16.
49. Zhang, S., G. Ji, and J. Han, *The positional and angular distribution of molecules flowing through cylindrical tube in free molecular flow.* Physics Procedia, 2012. **32**: p. 513-524.
50. Franz, G., *Plasma etch processes*, in *Low Pressure Plasmas and Microstructuring Technology*. 2009, Springer. p. 439-515.
51. Allain, J.P. and A. Shetty, *Unraveling atomic-level self-organization at the plasma-material interface.* Journal of Physics D: Applied Physics, 2017. **50**(28): p. 283002.
52. Coumou, D.J., et al., *Ion energy distribution skew control using phase-locked harmonic RF bias drive.* IEEE Transactions on Plasma Science, 2014. **42**(7): p. 1880-1893.
53. Cheng, E. and G.S. Hwang, *Dissociative chemisorption of methyl fluoride and its implications for atomic layer etching of silicon nitride.* Applied Surface Science, 2021. **543**: p. 148557.
54. Sridhar, S., P.L. Ventzek, and A. Ranjan, *Role of physisorption in atomic layer etching of silicon nitride.* Journal of Vacuum Science & Technology A: Vacuum, Surfaces, and Films, 2020. **38**(4): p. 043007.
55. Richey, N.E., C. De Paula, and S.F. Bent, *Understanding chemical and physical mechanisms in atomic layer deposition.* The journal of chemical physics, 2020. **152**(4): p. 040902.
56. Antoun, G., et al., *The role of physisorption in the cryogenic etching process of silicon.* Japanese Journal of Applied Physics, 2019. **58**(SE): p. SEEB03.
57. Antoun, G., et al., *Mechanism understanding in cryo atomic layer etching of SiO2 based upon C4F8 physisorption.* Scientific Reports, 2021. **11**(1): p. 1-10.
58. Lill, T., et al. *Emerging etching and patterning technologies: from concepts to practical applications*. in *48th international conference on Micro and Nano Engineering - Eurosensors (MNE-ES 2022)*. 2022. Leuven, Belgium.
59. Chen, D. and Q. Liu, *A novel hanging bowl-shaped mask for the fabrication of vertical sidewall structures.* Frontiers of Physics, 2016. **11**: p. 1-4.
60. Bobinac, J., et al., *Effect of Mask Geometry Variation on Plasma Etching Profiles.* Micromachines, 2023. **14**(3): p. 665.
61. Shumilov, A., I. Amirov, and V. Lukichev, *Modeling of the high aspect groove etching in Si in a Cl 2/Ar mixture plasma.* Russian Microelectronics, 2016. **45**: p. 167-179.

62. Paik, S.T., *Is the mean free path the mean of a distribution?* American Journal of Physics, 2014. **82**(6): p. 602-608.
63. Arellano, J. *Adsorption of formaldehyde on F@ graphene layer*. in *Journal of Physics: Conference Series*. 2022. IOP Publishing.

SUPPLEMENTARY MATERIAL

This document contains the supplementary material associated with the article “Assessing neutral transport mechanisms in aspect ratio dependent etching by means of experiments and multiscale plasma modeling” by Patrick Vanraes, Syam Parayil Venugopalan, Matthieu Besemer and Annemie Bogaerts in *Plasma Sources Science and Technology*.

S1. Surface chemistry set

Table S1. The surface reactions used in the surface chemistry set of MCFPM in the present work, as designed according to the principles described in our previous work in Ref. [1]. The probability p is a constant (energy-independent) reaction probability, used in the chemistry of neutral species. If it is used in an ion reaction, it needs to be rescaled relative to the competing energy-dependent reactions with the same reacting incident species and surface group, because the latter are given priority to the former. Energy-dependent reactions with a positive value of $p(E_{ref})$ have a probability of $p(E_i)f(\theta_i) = p(E_{ref})\frac{(E_i-E_{th})^a}{(E_{ref}-E_{th})^a}f(\theta_i)$, with E_i the kinetic energy of the incoming ion, E_{th} the threshold energy, $p(E_{ref})$ the reaction probability at a reference energy E_{ref}, a an exponent and $f(\theta_i)$ the angular dependency of the reaction probability. A negative value of $p(E_{ref})$ indicates a deposition reaction with an energy-dependent probability calculated as $p(E_i) = p(E_{ref})\ \frac{(E_{th}-E_i)}{E_{th}}$. PE and CE stand for the angular dependencies for physical etching and chemical etching, as explained in Ref. [1]. When $f(\theta_i)$ is not defined, the reaction probability is independent from the incident angle. Surface groups are indicated with an index (s), gas species containing ten units of the same species with an index (10) and gas species containing only one unit without an index. The reactions of CHF^+, CHF_2^+, CF_3^- and F^* are equal to the ones of CF^+, CF_2^+, CF_3^+ and F, respectively, and are therefore not mentioned in the table. The same counts for hot neutrals resulting from ion scattering of the surface, whose reactions are identical to the ones of the corresponding ions. The reactions of gas species containing one unit are also omitted from the table, because they are equal to the reactions of the corresponding gas species containing ten units, but with a 10 times lower reaction probability. As an exception, the surface interactions of CHF_3 are shown, serving as an example.

Surface reactions	p	E_{th} (eV)	$p(E_{ref})$	E_{ref} (eV)	a	$f(\theta_i)$
Ar^+ surface chemistry						
$PR_{(s)} + Ar^+ \rightarrow PR_{(10)} + Ar$		71.1	0.098	350	0.5	PE
$Si_{(s)} + Ar^+ \rightarrow Si_{(10)} + Ar$		71.1	0.046	350	0.5	PE
$SiF_{(s)} + Ar^+ \rightarrow SiF_{(10)} + Ar$		71.1	0.046	350	0.5	PE
$SiF_{2(s)} + Ar^+ \rightarrow SiF_{2(10)} + Ar$		71.1	0.092	350	0.5	PE
$SiF_{3(s)} + Ar^+ \rightarrow SiF_{3(10)} + Ar$		71.1	0.092	350	0.5	PE
$SiF_{4(s)} + Ar^+ \rightarrow SiF_{4(10)} + Ar$		0.01	0.60	350	1.0	CE
$SiO_{2(s)} + Ar^+ \rightarrow SiO_{2(10)} + Ar$		102	0.0084	150	1.0	PE
$C_{(s)} + Ar^+ \rightarrow C_{(10)} + Ar$		71.1	0.037	350	0.5	PE
$CF_{(s)} + Ar^+ \rightarrow CF_{(10)} + Ar$		71.1	0.037	350	0.5	PE
$CF_{2(s)} + Ar^+ \rightarrow CF_{2(10)} + Ar$		71.1	0.074	350	0.5	PE

Reaction						
$CF_{3(s)} + Ar^+ \rightarrow CF_{3(10)} + Ar$		71.1	0.074	350	0.5	PE
$CF_{4(s)} + Ar^+ \rightarrow CF_{4(10)} + Ar$		0.01	0.60	350	1.0	CE
$SiO_2C_{(s)} + Ar^+ \rightarrow Si_{(s)} + CO_{2(10)} + Ar$		25.0	0.13	130	0.5	PE
$SiO_2C_{(s)} + Ar^+ \rightarrow Si_{(10)} + CO_{2(10)} + Ar$		71.1	0.065	130	0.5	PE
$SiO_2CF_{(s)} + Ar^+ \rightarrow SiF_{(s)} + CO_{2(10)} + Ar$		25.0	0.13	130	0.5	PE
$SiO_2CF_{(s)} + Ar^+ \rightarrow SiF_{(10)} + CO_{2(10)} + Ar$		71.1	0.065	130	0.5	PE
$SiO_2CF_{2(s)} + Ar^+ \rightarrow SiF_{2(s)} + CO_{2(10)} + Ar$		25.0	0.065	130	0.5	PE
$SiO_2CF_{2(s)} + Ar^+ \rightarrow SiF_{2(10)} + CO_{2(10)} + Ar$		71.1	0.13	130	0.5	PE
$SiO_2CF_{3(s)} + Ar^+ \rightarrow SiF_{3(s)} + CO_{2(10)} + Ar$		25.0	0.065	130	0.5	PE
$SiO_2CF_{3(s)} + Ar^+ \rightarrow SiF_{3(10)} + CO_{2(10)} + Ar$		71.1	0.13	130	0.5	PE
$SiO_2CF_{4(s)} + Ar^+ \rightarrow SiF_{4(s)} + CO_{2(10)} + Ar$		25.0	0.065	130	0.5	PE
$SiO_2CF_{4(s)} + Ar^+ \rightarrow SiF_{4(10)} + CO_{2(10)} + Ar$		71.1	0.13	130	0.5	PE
F^+ surface chemistry						
$PR_{(s)} + F^+ \rightarrow PR_{(10)} + F$		45.7	0.0782	350	1.0	CE
$Si_{(s)} + F^+ \rightarrow SiF_{(10)}$		45.7	0.0128	350	1.0	CE
$Si_{(s)} + F^+ \rightarrow Si_{(10)} + F$		45.7	0.0237	350	1.0	CE
$Si_{(s)} + F^+ \rightarrow SiF_{(s)}$	0.085					
$SiF_{(s)} + F^+ \rightarrow SiF_{2(10)}$		58.9	0.0118	350	1.0	CE
$SiF_{(s)} + F^+ \rightarrow SiF_{(10)} + F$		58.9	0.0274	350	1.0	CE
$SiF_{(s)} + F^+ \rightarrow SiF_{2(s)}$	0.075					
$SiF_{2(s)} + F^+ \rightarrow SiF_{3(10)}$		49.4	0.0169	350	1.0	CE
$SiF_{2(s)} + F^+ \rightarrow SiF_{2(10)} + F$		49.4	0.0675	350	1.0	CE
$SiF_{2(s)} + F^+ \rightarrow SiF_{3(s)}$	0.045					
$SiF_{3(s)} + F^+ \rightarrow SiF_{3(10)} + F$		52.6	0.077	350	1.0	CE
$SiF_{3(s)} + F^+ \rightarrow SiF_{4(s)}$		450	-0.10			
$SiF_{4(s)} + F^+ \rightarrow SiF_{4(10)} + F$		0.01	0.50	350	1.0	CE
$SiO_{2(s)} + F^+ \rightarrow SiO_{2(10)} + F$		253	0.0108	350	1.0	CE
$SiO_{2(s)} + F^+ \rightarrow SiF_{(s)} + O_{2(10)}$	0.002					
$C_{(s)} + F^+ \rightarrow CF_{(10)}$		45.7	0.0103	350	1.0	CE
$C_{(s)} + F^+ \rightarrow C_{(10)} + F$		45.7	0.0191	350	1.0	CE
$C_{(s)} + F^+ \rightarrow CF_{(s)}$	0.085					
$CF_{(s)} + F^+ \rightarrow CF_{2(10)}$		58.9	0.0095	350	1.0	CE
$CF_{(s)} + F^+ \rightarrow CF_{(10)} + F$		58.9	0.0221	350	1.0	CE
$CF_{(s)} + F^+ \rightarrow CF_{2(s)}$	0.075					
$CF_{2(s)} + F^+ \rightarrow CF_{3(10)}$		49.4	0.0136	350	1.0	CE
$CF_{2(s)} + F^+ \rightarrow CF_{2(10)} + F$		49.4	0.0544	350	1.0	CE
$CF_{2(s)} + F^+ \rightarrow CF_{3(s)}$	0.045					
$CF_{3(s)} + F^+ \rightarrow CF_{3(10)} + F$		52.6	0.0621	350	1.0	CE
$CF_{3(s)} + F^+ \rightarrow CF_{4(s)}$		450	-0.081			
$CF_{4(s)} + F^+ \rightarrow CF_{4(10)} + F$		0.01	0.50	350	1.0	CE
$SiO_2C_{(s)} + F^+ \rightarrow Si_{(s)} + CO_{2(10)} + F$		25.0	0.101	130	0.5	CE
$SiO_2C_{(s)} + F^+ \rightarrow Si_{(10)} + CO_{2(10)} + F$		71.1	0.051	130	0.5	CE
$SiO_2CF_{(s)} + F^+ \rightarrow SiF_{(s)} + CO_{2(10)} + F$		25.0	0.101	130	0.5	CE

$SiO_2CF_{(s)} + F^+ \rightarrow SiF_{(10)} + CO_{2(10)} + F$		71.1	0.051	130	0.5	CE
$SiO_2CF_{2(s)} + F^+ \rightarrow SiF_{2(s)} + CO_{2(10)} + F$		25.0	0.051	130	0.5	CE
$SiO_2CF_{2(s)} + F^+ \rightarrow SiF_{2(10)} + CO_{2(10)} + F$		71.1	0.101	130	0.5	CE
$SiO_2CF_{3(s)} + F^+ \rightarrow SiF_{3(s)} + CO_{2(10)} + F$		25.0	0.051	130	0.5	CE
$SiO_2CF_{3(s)} + F^+ \rightarrow SiF_{3(10)} + CO_{2(10)} + F$		71.1	0.101	130	0.5	CE
$SiO_2CF_{4(s)} + F^+ \rightarrow SiF_{4(s)} + CO_{2(10)} + F$		25.0	0.051	130	0.5	CE
$SiO_2CF_{4(s)} + F^+ \rightarrow SiF_{4(10)} + CO_{2(10)} + F$		71.1	0.101	130	0.5	CE
F_2^+ surface chemistry						
$PR_{(s)} + F_2^+ \rightarrow PR_{(10)} + 2F$		91.4	0.1564	700	1.0	CE
$Si_{(s)} + F_2^+ \rightarrow SiF_{(10)}$		91.4	0.0256	700	1.0	CE
$Si_{(s)} + F_2^+ \rightarrow Si_{(10)} + 2F$		91.4	0.0474	700	1.0	CE
$Si_{(s)} + F_2^+ \rightarrow SiF_{(s)}$	0.17					
$SiF_{(s)} + F_2^+ \rightarrow SiF_{2(10)}$		117.8	0.0236	700	1.0	CE
$SiF_{(s)} + F_2^+ \rightarrow SiF_{(10)} + 2F$		117.8	0.0548	700	1.0	CE
$SiF_{(s)} + F_2^+ \rightarrow SiF_{2(s)}$	0.15					
$SiF_{2(s)} + F_2^+ \rightarrow SiF_{3(10)}$		98.8	0.0338	700	1.0	CE
$SiF_{2(s)} + F_2^+ \rightarrow SiF_{2(10)} + 2F$		98.8	0.135	700	1.0	CE
$SiF_{2(s)} + F_2^+ \rightarrow SiF_{3(s)}$	0.09					
$SiF_{3(s)} + F_2^+ \rightarrow SiF_{3(10)} + 2F$		105.2	0.154	700	1.0	CE
$SiF_{3(s)} + F_2^+ \rightarrow SiF_{4(s)}$		900	-0.20			
$SiF_{4(s)} + F_2^+ \rightarrow SiF_{4(10)} + 2F$		0.01	0.60	700	1.0	CE
$SiO_{2(s)} + F_2^+ \rightarrow SiO_{2(10)} + 2F$		506	0.0216	700	1.0	CE
$SiO_{2(s)} + F_2^+ \rightarrow SiF_{(s)} + O_{2(10)}$	0.004					
$C_{(s)} + F_2^+ \rightarrow CF_{(10)}$		91.4	0.0206	700	1.0	CE
$C_{(s)} + F_2^+ \rightarrow C_{(10)} + 2F$		91.4	0.0382	700	1.0	CE
$C_{(s)} + F_2^+ \rightarrow CF_{(s)}$	0.17					
$CF_{(s)} + F_2^+ \rightarrow CF_{2(10)}$		117.8	0.0190	700	1.0	CE
$CF_{(s)} + F_2^+ \rightarrow CF_{(10)} + 2F$		117.8	0.0442	700	1.0	CE
$CF_{(s)} + F_2^+ \rightarrow CF_{2(s)}$	0.15					
$CF_{2(s)} + F_2^+ \rightarrow CF_{3(10)}$		98.8	0.0272	700	1.0	CE
$CF_{2(s)} + F_2^+ \rightarrow CF_{2(10)} + 2F$		98.8	0.1088	700	1.0	CE
$CF_{2(s)} + F_2^+ \rightarrow CF_{3(s)}$	0.09					
$CF_{3(s)} + F_2^+ \rightarrow CF_{3(10)} + 2F$		105.2	0.1242	700	1.0	CE
$CF_{3(s)} + F_2^+ \rightarrow CF_{4(s)}$		900	-0.162			
$CF_{4(s)} + F_2^+ \rightarrow CF_{4(10)} + 2F$		0.01	0.60	700	1.0	CE
$SiO_2C_{(s)} + F_2^+ \rightarrow Si_{(s)} + CO_{2(10)} + 2F$		50.0	0.203	260	0.5	CE
$SiO_2C_{(s)} + F_2^+ \rightarrow Si_{(10)} + CO_{2(10)} + 2F$		142	0.101	260	0.5	CE
$SiO_2CF_{(s)} + F_2^+ \rightarrow SiF_{(s)} + CO_{2(10)} + 2F$		50.0	0.203	260	0.5	CE
$SiO_2CF_{(s)} + F_2^+ \rightarrow SiF_{(10)} + CO_{2(10)} + 2F$		142	0.101	260	0.5	CE
$SiO_2CF_{2(s)} + F_2^+ \rightarrow SiF_{2(s)} + CO_{2(10)} + 2F$		50.0	0.101	260	0.5	CE
$SiO_2CF_{2(s)} + F_2^+ \rightarrow SiF_{2(10)} + CO_{2(10)} + 2F$		142	0.203	260	0.5	CE
$SiO_2CF_{3(s)} + F_2^+ \rightarrow SiF_{3(s)} + CO_{2(10)} + 2F$		50.0	0.101	260	0.5	CE
$SiO_2CF_{3(s)} + F_2^+ \rightarrow SiF_{3(10)} + CO_{2(10)} + 2F$		142	0.203	260	0.5	CE

Reaction						
$SiO_2CF_{4(s)} + F_2^+ \rightarrow SiF_{4(s)} + CO_{2(10)} + 2F$		50.0	0.101	260	0.5	CE
$SiO_2CF_{4(s)} + F_2^+ \rightarrow SiF_{4(10)} + CO_{2(10)} + 2F$		142	0.203	260	0.5	CE
CF^+ surface chemistry						
$PR_{(s)} + CF^+ \rightarrow C_{(s)} + PR_{(10)} + F$		76.2	0.0782	583	1.0	CE
$PR_{(s)} + CF^+ \rightarrow PR_{(s)} + CF$	0.085					
$Si_{(s)} + CF^+ \rightarrow C_{(s)} + SiF_{(10)}$		76.2	0.0128	583	1.0	CE
$Si_{(s)} + CF^+ \rightarrow C_{(s)} + Si_{(10)} + F$		76.2	0.0237	583	1.0	CE
$Si_{(s)} + CF^+ \rightarrow SiF_{(s)} + C$	0.085					
$SiF_{(s)} + CF^+ \rightarrow C_{(s)} + SiF_{2(10)}$		98.2	0.0118	583	1.0	CE
$SiF_{(s)} + CF^+ \rightarrow C_{(s)} + SiF_{(10)} + F$		98.2	0.0274	583	1.0	CE
$SiF_{(s)} + CF^+ \rightarrow SiF_{2(s)} + C$	0.075					
$SiF_{2(s)} + CF^+ \rightarrow C_{(s)} + SiF_{3(10)}$		82.3	0.0169	583	1.0	CE
$SiF_{2(s)} + CF^+ \rightarrow C_{(s)} + SiF_{2(10)} + F$		82.3	0.0675	583	1.0	CE
$SiF_{2(s)} + CF^+ \rightarrow SiF_{3(s)} + C$	0.045					
$SiF_{3(s)} + CF^+ \rightarrow C_{(s)} + SiF_{3(10)} + F$		87.7	0.077	583	1.0	CE
$SiF_{3(s)} + CF^+ \rightarrow SiF_{4(s)} + C$		750	-0.10			CE
$SiF_{4(s)} + CF^+ \rightarrow SiF_{4(10)} + C + F$		0.01	0.56	350	1.0	CE
$SiO_{2(s)} + CF^+ \rightarrow SiF_{(10)} + CO_{2(10)}$		221	0.0373	350	1.0	CE
$SiO_{2(s)} + CF^+ \rightarrow SiO_2CF_{(s)}$		221	-0.1282			
$C_{(s)} + CF^+ \rightarrow C_{(s)} + CF_{(10)}$		76.2	0.0103	583	1.0	CE
$C_{(s)} + CF^+ \rightarrow C_{(s)} + C_{(10)} + F$		76.2	0.0191	583	1.0	CE
$C_{(s)} + CF^+ \rightarrow CF_{(s)} + C$	0.085					
$CF_{(s)} + CF^+ \rightarrow C_{(s)} + CF_{2(10)}$		98.2	0.0095	583	1.0	CE
$CF_{(s)} + CF^+ \rightarrow C_{(s)} + CF_{(10)} + F$		98.2	0.0221	583	1.0	CE
$CF_{(s)} + CF^+ \rightarrow CF_{2(s)} + C$	0.075					
$CF_{2(s)} + CF^+ \rightarrow C_{(s)} + CF_{3(10)}$		82.3	0.0136	583	1.0	CE
$CF_{2(s)} + CF^+ \rightarrow C_{(s)} + CF_{2(10)} + F$		82.3	0.0544	583	1.0	CE
$CF_{2(s)} + CF^+ \rightarrow CF_{3(s)} + C$	0.045					
$CF_{3(s)} + CF^+ \rightarrow C_{(s)} + CF_{3(10)} + F$		87.7	0.0621	583	1.0	CE
$CF_{3(s)} + CF^+ \rightarrow CF_{4(s)} + C$		750	-0.081			CE
$CF_{4(s)} + CF^+ \rightarrow CF_{4(10)} + C + F$		0.01	0.56	350	1.0	CE
$SiO_2C_{(s)} + CF^+ \rightarrow SiF_{(10)} + CO_{2(10)} + C$		221	0.0311	350	1.0	PE
$SiO_2C_{(s)} + CF^+ \rightarrow SiO_2CF_{(s)} + C$		221	-0.128			CE
$SiO_2CF_{(s)} + CF^+ \rightarrow SiF_{2(10)} + CO_{2(10)} + C$		221	0.0246	350	1.0	PE
$SiO_2CF_{(s)} + CF^+ \rightarrow SiO_2C_{(s)} + CF_{(s)} + F$		221	-0.128			CE
$SiO_2CF_{2(s)} + CF^+ \rightarrow SiF_{3(10)} + CO_{2(10)} + C$		221	0.0203	350	1.0	PE
$SiO_2CF_{2(s)} + CF^+ \rightarrow SiO_2CF_{(s)} + CF_{(s)} + F$		221	-0.128			CE
$SiO_2CF_{3(s)} + CF^+ \rightarrow SiF_{4(10)} + CO_{2(10)} + C$		221	0.0173	350	1.0	PE
$SiO_2CF_{3(s)} + CF^+ \rightarrow SiO_2CF_{2(s)} + CF_{(s)} + F$		221	-0.128			CE
$SiO_2CF_{4(s)} + CF^+ \rightarrow SiF_{4(10)} + CO_{2(10)} + CF$		221	0.0151	350	1.0	PE
$SiO_2CF_{4(s)} + CF^+ \rightarrow SiO_2CF_{3(s)} + CF_{(s)} + F$		221	-0.128			CE
CF_2^+ surface chemistry						

$PR_{(s)} + CF_2^+ \rightarrow PR_{(10)} + C + 2F$		121.9	0.0548	933	1.0	CE
$Si_{(s)} + CF_2^+ \rightarrow SiF_{(10)} + C$		121.9	0.0256	933	1.0	CE
$Si_{(s)} + CF_2^+ \rightarrow C_{(s)} + Si_{(10)} + 2F$		121.9	0.0474	933	1.0	CE
$Si_{(s)} + CF_2^+ \rightarrow SiF_{(s)} + C$	0.17					
$SiF_{(s)} + CF_2^+ \rightarrow SiF_{2(10)} + C$		157.1	0.0236	933	1.0	CE
$SiF_{(s)} + CF_2^+ \rightarrow C_{(s)} + SiF_{(10)} + 2F$		157.1	0.0548	933	1.0	CE
$SiF_{(s)} + CF_2^+ \rightarrow SiF_{2(s)} + C$	0.15					
$SiF_{2(s)} + CF_2^+ \rightarrow C_{(s)} + SiF_{3(10)}$		131.7	0.0338	933	1.0	CE
$SiF_{2(s)} + CF_2^+ \rightarrow SiF_{2(10)} + C + 2F$		131.7	0.135	933	1.0	CE
$SiF_{2(s)} + CF_2^+ \rightarrow SiF_{3(s)} + C$	0.09					
$SiF_{3(s)} + CF_2^+ \rightarrow C_{(s)} + SiF_{3(10)} + 2F$		140.3	0.060	933	1.0	CE
$SiF_{3(s)} + CF_2^+ \rightarrow SiF_{3(10)} + C + 2F$		140.3	0.094	933	1.0	CE
$SiF_{3(s)} + CF_2^+ \rightarrow SiF_{4(s)} + C$		1200	-0.20			
$SiF_{4(s)} + CF_2^+ \rightarrow SiF_{4(10)} + C + 2F$		0.01	0.65	350	1.0	CE
$SiO_{2(s)} + CF_2^+ \rightarrow SiF_{2(10)} + CO_{2(10)}$		106	0.0731	350	0.5	CE
$SiO_{2(s)} + CF_2^+ \rightarrow SiO_2CF_{2(s)}$		106	-0.0871			CE
$C_{(s)} + CF_2^+ \rightarrow CF_{(10)}$		121.9	0.0206	933	1.0	CE
$C_{(s)} + CF_2^+ \rightarrow C_{(s)} + C_{(10)} + 2F$		121.9	0.0382	933	1.0	CE
$C_{(s)} + CF_2^+ \rightarrow CF_{(s)}$	0.17					
$CF_{(s)} + CF_2^+ \rightarrow CF_{2(10)}$		157.1	0.0190	933	1.0	CE
$CF_{(s)} + CF_2^+ \rightarrow C_{(s)} + CF_{(10)} + 2F$		157.1	0.0442	933	1.0	CE
$CF_{(s)} + CF_2^+ \rightarrow CF_{2(s)}$	0.15					
$CF_{2(s)} + CF_2^+ \rightarrow C_{(s)} + CF_{3(10)}$		131.7	0.0272	933	1.0	CE
$CF_{2(s)} + CF_2^+ \rightarrow CF_{2(10)} + 2F$		131.7	0.1088	933	1.0	CE
$CF_{2(s)} + CF_2^+ \rightarrow CF_{3(s)}$	0.09					
$CF_{3(s)} + CF_2^+ \rightarrow C_{(s)} + CF_{3(10)} + 2F$		140.3	0.0600	933	1.0	CE
$CF_{3(s)} + CF_2^+ \rightarrow CF_{3(10)} + C + 2F$		140.3	0.0642	933	1.0	
$CF_{3(s)} + CF_2^+ \rightarrow CF_{4(s)}$		1200	-0.162			
$CF_{4(s)} + CF_2^+ \rightarrow CF_{4(10)} + C + 2F$		0.01	0.65	350	1.0	CE
$SiO_2C_{(s)} + CF_2^+ \rightarrow SiF_{2(s)} + CO_{2(10)} + C$		106	0.0609	350	0.5	PE
$SiO_2C_{(s)} + CF_2^+ \rightarrow SiO_2C_{(s)} + CF_{2(s)}$		106	-0.0871			CE
$SiO_2CF_{(s)} + CF_2^+ \rightarrow SiF_{3(s)} + CO_{2(10)} + C$		106	0.0482	350	0.5	PE
$SiO_2CF_{(s)} + CF_2^+ \rightarrow SiO_2C_{(s)} + CF_{3(s)}$		106	-0.0871			CE
$SiO_2CF_{2(s)} + CF_2^+ \rightarrow SiF_{4(s)} + CO_{2(10)} + C$		106	0.0399	350	0.5	PE
$SiO_2CF_{2(s)} + CF_2^+ \rightarrow SiO_2CF_{(s)} + CF_{3(s)}$		106	-0.0871			CE
$SiO_2CF_{3(s)} + CF_2^+ \rightarrow SiF_{4(s)} + CO_{2(10)} + CF$		106	0.0340	350	0.5	PE
$SiO_2CF_{3(s)} + CF_2^+ \rightarrow SiO_2CF_{2(s)} + CF_{3(s)}$		106	-0.0871			CE
$SiO_2CF_{4(s)} + CF_2^+ \rightarrow SiF_{4(s)} + CO_{2(10)} + CF_2$		106	0.0296	350	0.5	PE
$SiO_2CF_{4(s)} + CF_2^+ \rightarrow SiO_2CF_{3(s)} + CF_{3(s)}$		106	-0.0871			CE
CF_3^+ surface chemistry						
$PR_{(s)} + CF_3^+ \rightarrow PR_{(10)} + C + 3F$		167.6	0.1524	1283	1.0	CE
$Si_{(s)} + CF_3^+ \rightarrow C_{(s)} + SiF_{(10)}$		167.6	0.0384	1283	1.0	CE
$Si_{(s)} + CF_3^+ \rightarrow Si_{(10)} + C + 3F$		167.6	0.0711	1283	1.0	CE

$Si_{(s)} + CF_3^+ \rightarrow SiF_{(s)} + C$	0.085					
$SiF_{(s)} + CF_3^+ \rightarrow C_{(s)} + SiF_{2(10)}$		216	0.0354	1283	1.0	CE
$SiF_{(s)} + CF_3^+ \rightarrow SiF_{(10)} + C + 3F$		216	0.0822	1283	1.0	CE
$SiF_{(s)} + CF_3^+ \rightarrow SiF_{2(s)} + C$	0.075					
$SiF_{2(s)} + CF_3^+ \rightarrow C_{(s)} + SiF_{3(10)}$		181.1	0.0507	1283	1.0	CE
$SiF_{2(s)} + CF_3^+ \rightarrow SiF_{2(10)} + C + 3F$		181.1	0.2025	1283	1.0	CE
$SiF_{2(s)} + CF_3^+ \rightarrow SiF_{3(s)} + C$	0.045					
$SiF_{3(s)} + CF_3^+ \rightarrow C_{(s)} + SiF_{3(10)} + 3F$		192.9	0.060	1283	1.0	CE
$SiF_{3(s)} + CF_3^+ \rightarrow SiF_{3(10)} + C + 3F$		192.9	0.171	1283	1.0	CE
$SiF_{3(s)} + CF_3^+ \rightarrow SiF_{4(s)} + C$		1650	-0.30			
$SiF_{4(s)} + CF_3^+ \rightarrow SiF_{4(10)} + C + 3F$		0.01	0.75	350	1.0	CE
$SiO_{2(s)} + CF_3^+ \rightarrow SiF_{3(10)} + CO_{2(10)}$		108	0.0204	150	1.0	CE
$SiO_{2(s)} + CF_3^+ \rightarrow SiO_2CF_{3(s)}$		108	-0.046			CE
$C_{(s)} + CF_3^+ \rightarrow C_{(s)} + CF_{(10)}$		167.6	0.0309	1283	1.0	CE
$C_{(s)} + CF_3^+ \rightarrow C_{(10)} + C + 3F$		167.6	0.0573	1283	1.0	CE
$C_{(s)} + CF_3^+ \rightarrow CF_{(s)} + C$	0.085					
$CF_{(s)} + CF_3^+ \rightarrow C_{(s)} + CF_{2(10)}$		216	0.0285	1283	1.0	CE
$CF_{(s)} + CF_3^+ \rightarrow CF_{(10)} + C + 3F$		216	0.0663	1283	1.0	CE
$CF_{(s)} + CF_3^+ \rightarrow CF_{2(s)} + C$	0.075					
$CF_{2(s)} + CF_3^+ \rightarrow C_{(s)} + CF_{3(10)}$		181.1	0.0408	1283	1.0	CE
$CF_{2(s)} + CF_3^+ \rightarrow CF_{2(10)} + C + 3F$		181.1	0.1632	1283	1.0	CE
$CF_{2(s)} + CF_3^+ \rightarrow CF_{3(s)} + C$	0.045					
$CF_{3(s)} + CF_3^+ \rightarrow C_{(s)} + CF_{3(10)} + 3F$		192.9	0.0600	1283	1.0	CE
$CF_{3(s)} + CF_3^+ \rightarrow CF_{3(10)} + C + 3F$		192.9	0.1263	1283	1.0	
$CF_{3(s)} + CF_3^+ \rightarrow CF_{4(s)} + C$		1650	-0.243			
$CF_{4(s)} + CF_3^+ \rightarrow CF_{4(10)} + C + 3F$		0.01	0.75	350	1.0	CE
$SiO_2C_{(s)} + CF_3^+ \rightarrow SiF_{3(s)} + CO_{2(10)} + C$		108	0.0170	150	1.0	PE
$SiO_2C_{(s)} + CF_3^+ \rightarrow SiO_2C_{(s)} + CF_{3(s)}$		108	-0.046			PE
$SiO_2CF_{(s)} + CF_3^+ \rightarrow SiF_{4(s)} + CO_{2(10)} + C$		108	0.0134	150	1.0	PE
$SiO_2CF_{(s)} + CF_3^+ \rightarrow SiO_2CF_{(s)} + CF_{3(s)}$		108	-0.046			PE
$SiO_2CF_{2(s)} + CF_3^+ \rightarrow SiF_{4(s)} + CO_{2(10)} + CF$		108	0.0111	150	1.0	PE
$SiO_2CF_{2(s)} + CF_3^+ \rightarrow SiO_2CF_{2(s)} + CF_{3(s)}$		108	-0.046			PE
$SiO_2CF_{3(s)} + CF_3^+ \rightarrow SiF_{4(s)} + CO_{2(10)} + CF_2$		108	0.0095	150	1.0	PE
$SiO_2CF_{3(s)} + CF_3^+ \rightarrow SiO_2CF_{3(s)} + CF_{3(s)}$		108	-0.046			PE
$SiO_2CF_{4(s)} + CF_3^+ \rightarrow SiF_{4(s)} + CO_{2(10)} + CF_3$		108	0.0083	150	1.0	PE
$SiO_2CF_{4(s)} + CF_3^+ \rightarrow SiO_2CF_{4(s)} + CF_{3(s)}$		108	-0.046			PE
$Si_{(10)}$ surface chemistry						
$PR_{(s)} + Si_{(10)} \rightarrow PR_{(s)} + Si_{(10)}$	1.0					
$Si_{(s)} + Si_{(10)} \rightarrow Si_{(s)} + Si_{(s)}$	1.0					
$SiF_{(s)} + Si_{(10)} \rightarrow Si_{(s)} + SiF_{(s)}$	1.0					
$SiF_{2(s)} + Si_{(10)} \rightarrow SiF_{(s)} + SiF_{(s)}$	0.41					
$SiF_{3(s)} + Si_{(10)} \rightarrow SiF_{2(s)} + SiF_{(s)}$	0.20					
$SiF_{4(s)} + Si_{(10)} \rightarrow SiF_{4(s)} + Si_{(10)}$	1.0					

$SiO_{2(s)} + Si_{(10)} \rightarrow SiO_{2(s)} + Si_{(s)}$	0.1	
$C_{(s)} + Si_{(10)} \rightarrow C_{(s)} + Si_{(s)}$	1.0	
$CF_{(s)} + Si_{(10)} \rightarrow C_{(s)} + SiF_{(s)}$	1.0	
$CF_{2(s)} + Si_{(10)} \rightarrow CF_{(s)} + SiF_{(s)}$	0.51	
$CF_{3(s)} + Si_{(10)} \rightarrow CF_{2(s)} + SiF_{(s)}$	0.25	
$CF_{4(s)} + Si_{(10)} \rightarrow CF_{4(s)} + Si_{(10)}$	1.0	
$SiO_2C_{(s)} + Si_{(10)} \rightarrow SiO_2C_{(s)} + Si_{(s)}$	1.0	
$SiO_2CF_{(s)} + Si_{(10)} \rightarrow SiO_2C_{(s)} + SiF_{(s)}$	1.0	
$SiO_2CF_{2(s)} + Si_{(10)} \rightarrow SiO_2CF_{(s)} + SiF_{(s)}$	0.51	
$SiO_2CF_{3(s)} + Si_{(10)} \rightarrow SiO_2CF_{2(s)} + SiF_{(s)}$	0.25	
$SiO_2CF_{4(s)} + Si_{(10)} \rightarrow SiO_2CF_{4(s)} + Si_{(10)}$	1.0	
$SiF_{(10)}$ surface chemistry		
$PR_{(s)} + SiF_{(10)} \rightarrow PR_{(s)} + SiF_{(10)}$	1.0	
$Si_{(s)} + SiF_{(10)} \rightarrow Si_{(s)} + SiF_{(s)}$	0.88	
$SiF_{(s)} + SiF_{(10)} \rightarrow Si_{(s)} + SiF_{2(s)}$	0.60	
$SiF_{2(s)} + SiF_{(10)} \rightarrow SiF_{(s)} + SiF_{2(s)}$	0.20	
$SiF_{3(s)} + SiF_{(10)} \rightarrow SiF_{2(s)} + SiF_{2(s)}$	0.10	
$SiF_{4(s)} + SiF_{(10)} \rightarrow SiF_{4(s)} + SiF_{(10)}$	1.0	
$SiO_{2(s)} + SiF_{(10)} \rightarrow SiO_{2(s)} + SiF_{(s)}$	0.095	
$C_{(s)} + SiF_{(10)} \rightarrow C_{(s)} + SiF_{(s)}$	0.99	
$CF_{(s)} + SiF_{(10)} \rightarrow C_{(s)} + SiF_{2(s)}$	0.70	
$CF_{2(s)} + SiF_{(10)} \rightarrow CF_{(s)} + SiF_{2(s)}$	0.25	
$CF_{3(s)} + SiF_{(10)} \rightarrow CF_{2(s)} + SiF_{2(s)}$	0.13	
$CF_{4(s)} + SiF_{(10)} \rightarrow CF_{4(s)} + SiF_{(10)}$	1.0	
$SiO_2C_{(s)} + SiF_{(10)} \rightarrow SiO_2C_{(s)} + SiF_{(s)}$	0.99	
$SiO_2CF_{(s)} + SiF_{(10)} \rightarrow SiO_2C_{(s)} + SiF_{2(s)}$	0.70	
$SiO_2CF_{2(s)} + SiF_{(10)} \rightarrow SiO_2CF_{(s)} + SiF_{2(s)}$	0.25	
$SiO_2CF_{3(s)} + SiF_{(10)} \rightarrow SiO_2CF_{2(s)} + SiF_{2(s)}$	0.13	
$SiO_2CF_{4(s)} + SiF_{(10)} \rightarrow SiO_2CF_{4(s)} + SiF_{(10)}$	1.0	
$SiF_{2(10)}$ surface chemistry		
$PR_{(s)} + SiF_{2(10)} \rightarrow PR_{(s)} + SiF_{2(10)}$	1.0	
$Si_{(s)} + SiF_{2(10)} \rightarrow Si_{(s)} + SiF_{2(s)}$	0.75	
$SiF_{(s)} + SiF_{2(10)} \rightarrow Si_{(s)} + SiF_{3(s)}$	0.30	
$SiF_{2(s)} + SiF_{2(10)} \rightarrow SiF_{(s)} + SiF_{3(s)}$	0.10	
$SiF_{3(s)} + SiF_{2(10)} \rightarrow SiF_{2(s)} + SiF_{3(s)}$	0.05	
$SiF_{4(s)} + SiF_{2(10)} \rightarrow SiF_{4(s)} + SiF_{2(10)}$	1.0	
$SiO_{2(s)} + SiF_{2(10)} \rightarrow SiO_{2(s)} + SiF_{2(s)}$	0.090	
$C_{(s)} + SiF_{2(10)} \rightarrow C_{(s)} + SiF_{2(s)}$	0.90	
$CF_{(s)} + SiF_{2(10)} \rightarrow C_{(s)} + SiF_{3(s)}$	0.40	
$CF_{2(s)} + SiF_{2(10)} \rightarrow CF_{(s)} + SiF_{3(s)}$	0.15	
$CF_{3(s)} + SiF_{2(10)} \rightarrow CF_{2(s)} + SiF_{3(s)}$	0.08	
$CF_{4(s)} + SiF_{2(10)} \rightarrow CF_{4(s)} + SiF_{2(10)}$	1.0	

$SiO_2C_{(s)} + SiF_{2(10)} \rightarrow SiO_2C_{(s)} + SiF_{2(s)}$	0.90	
$SiO_2CF_{(s)} + SiF_{2(10)} \rightarrow SiO_2C_{(s)} + SiF_{3(s)}$	0.40	
$SiO_2CF_{2(s)} + SiF_{2(10)} \rightarrow SiO_2CF_{(s)} + SiF_{3(s)}$	0.15	
$SiO_2CF_{3(s)} + SiF_{2(10)} \rightarrow SiO_2CF_{2(s)} + SiF_{3(s)}$	0.08	
$SiO_2CF_{4(s)} + SiF_{2(10)} \rightarrow SiO_2CF_{4(s)} + SiF_{2(10)}$	1.0	
$SiF_{3(10)}$ surface chemistry		
$PR_{(s)} + SiF_{3(10)} \rightarrow PR_{(s)} + SiF_{3(10)}$	1.0	
$Si_{(s)} + SiF_{3(10)} \rightarrow Si_{(s)} + SiF_{3(s)}$	0.65	
$SiF_{(s)} + SiF_{3(10)} \rightarrow Si_{(s)} + SiF_{4(s)}$	0.15	
$SiF_{2(s)} + SiF_{3(10)} \rightarrow SiF_{(s)} + SiF_{4(s)}$	0.05	
$SiF_{3(s)} + SiF_{3(10)} \rightarrow SiF_{2(s)} + SiF_{4(s)}$	0.02	
$SiF_{4(s)} + SiF_{3(10)} \rightarrow SiF_{4(s)} + SiF_{3(10)}$	1.0	
$SiO_{2(s)} + SiF_{3(10)} \rightarrow SiO_{2(s)} + SiF_{3(s)}$	0.085	
$C_{(s)} + SiF_{3(10)} \rightarrow C_{(s)} + SiF_{3(s)}$	0.77	
$CF_{(s)} + SiF_{3(10)} \rightarrow C_{(s)} + SiF_{4(s)}$	0.20	
$CF_{2(s)} + SiF_{3(10)} \rightarrow CF_{(s)} + SiF_{4(s)}$	0.07	
$CF_{3(s)} + SiF_{3(10)} \rightarrow CF_{2(s)} + SiF_{4(s)}$	0.023	
$CF_{4(s)} + SiF_{3(10)} \rightarrow CF_{4(s)} + SiF_{3(10)}$	1.0	
$SiO_2C_{(s)} + SiF_{3(10)} \rightarrow SiO_2C_{(s)} + SiF_{3(s)}$	0.77	
$SiO_2CF_{(s)} + SiF_{3(10)} \rightarrow SiO_2C_{(s)} + SiF_{4(s)}$	0.20	
$SiO_2CF_{2(s)} + SiF_{3(10)} \rightarrow SiO_2CF_{(s)} + SiF_{4(s)}$	0.07	
$SiO_2CF_{3(s)} + SiF_{3(10)} \rightarrow SiO_2CF_{2(s)} + SiF_{4(s)}$	0.023	
$SiO_2CF_{4(s)} + SiF_{3(10)} \rightarrow SiO_2CF_{4(s)} + SiF_{3(10)}$	1.0	
$SiF_{4(10)}$ surface chemistry		
$PR_{(s)} + SiF_{4(10)} \rightarrow PR_{(s)} + SiF_{4(10)}$	1.0	
$Si_{(s)} + SiF_{4(10)} \rightarrow Si_{(s)} + SiF_{4(s)}$	0.05	
$SiF_{(s)} + SiF_{4(10)} \rightarrow SiF_{(s)} + SiF_{4(s)}$	0.05	
$SiF_{2(s)} + SiF_{4(10)} \rightarrow SiF_{2(s)} + SiF_{4(s)}$	0.02	
$SiF_{3(s)} + SiF_{4(10)} \rightarrow SiF_{3(s)} + SiF_{4(s)}$	0.02	
$SiF_{4(s)} + SiF_{4(10)} \rightarrow SiF_{4(s)} + SiF_{4(10)}$	1.0	
$SiO_{2(s)} + SiF_{4(10)} \rightarrow SiO_{2(s)} + SiF_{4(s)}$	0.05	
$C_{(s)} + SiF_{4(10)} \rightarrow C_{(s)} + SiF_{4(s)}$	0.05	
$CF_{(s)} + SiF_{4(10)} \rightarrow CF_{(s)} + SiF_{4(s)}$	0.05	
$CF_{2(s)} + SiF_{4(10)} \rightarrow CF_{2(s)} + SiF_{4(s)}$	0.02	
$CF_{3(s)} + SiF_{4(10)} \rightarrow CF_{3(s)} + SiF_{4(s)}$	0.02	
$CF_{4(s)} + SiF_{4(10)} \rightarrow CF_{4(s)} + SiF_{4(10)}$	1.0	
$SiO_2C_{(s)} + SiF_{4(10)} \rightarrow SiO_2C_{(s)} + SiF_{4(s)}$	0.05	
$SiO_2CF_{(s)} + SiF_{4(10)} \rightarrow SiO_2CF_{(s)} + SiF_{4(s)}$	0.05	
$SiO_2CF_{2(s)} + SiF_{4(10)} \rightarrow SiO_2CF_{2(s)} + SiF_{4(s)}$	0.02	
$SiO_2CF_{3(s)} + SiF_{4(10)} \rightarrow SiO_2CF_{3(s)} + SiF_{4(s)}$	0.02	
$SiO_2CF_{4(s)} + SiF_{4(10)} \rightarrow SiO_2CF_{4(s)} + SiF_{4(10)}$	1.0	

$SiO_{2(10)}$ surface chemistry		
$PR_{(s)} + SiO_{2(10)} \rightarrow PR_{(s)} + SiO_{2(10)}$	1.0	
$Si_{(s)} + SiO_{2(10)} \rightarrow Si_{(s)} + SiO_{2(s)}$	1.0	
$SiF_{(s)} + SiO_{2(10)} \rightarrow SiF_{(s)} + SiO_{2(s)}$	1.0	
$SiF_{2(s)} + SiO_{2(10)} \rightarrow SiF_{2(s)} + SiO_{2(s)}$	0.41	
$SiF_{3(s)} + SiO_{2(10)} \rightarrow SiF_{3(s)} + SiO_{2(s)}$	0.20	
$SiF_{4(s)} + SiO_{2(10)} \rightarrow SiF_{4(s)} + SiO_{2(10)}$	1.0	
$SiO_{2(s)} + SiO_{2(10)} \rightarrow SiO_{2(s)} + SiO_{2(s)}$	1.0	
$C_{(s)} + SiO_{2(10)} \rightarrow SiO_2C_{(s)}$	1.0	
$CF_{(s)} + SiO_{2(10)} \rightarrow SiO_2CF_{(s)}$	1.0	
$CF_{2(s)} + SiO_{2(10)} \rightarrow SiO_2CF_{2(s)}$	0.51	
$CF_{3(s)} + SiO_{2(10)} \rightarrow SiO_2CF_{3(s)}$	0.25	
$CF_{4(s)} + SiO_{2(10)} \rightarrow CF_{4(s)} + SiO_{2(10)}$	1.0	
$SiO_2C_{(s)} + SiO_{2(10)} \rightarrow SiO_2C_{(s)} + SiO_{2(s)}$	1.0	
$SiO_2CF_{(s)} + SiO_{2(10)} \rightarrow SiO_2CF_{(s)} + SiO_{2(s)}$	1.0	
$SiO_2CF_{2(s)} + SiO_{2(10)} \rightarrow SiO_2CF_{2(s)} + SiO_{2(s)}$	0.51	
$SiO_2CF_{3(s)} + SiO_{2(10)} \rightarrow SiO_2CF_{3(s)} + SiO_{2(s)}$	0.25	
$SiO_2CF_{4(s)} + SiO_{2(10)} \rightarrow SiO_2CF_{4(s)} + SiO_{2(10)}$	1.0	
F surface chemistry		
$PR_{(s)} + F \rightarrow PR_{(s)} + F$	1.0	
$Si_{(s)} + F \rightarrow SiF_{(s)}$	0.098	
$SiF_{(s)} + F \rightarrow SiF_{2(s)}$	0.092	
$SiF_{2(s)} + F \rightarrow SiF_{3(s)}$	0.059	
$SiF_{3(s)} + F \rightarrow SiF_{4(10)}$	0.0028	
$SiF_{3(s)} + F \rightarrow SiF_{4(s)}$	0.0202	
$SiF_{4(s)} + F \rightarrow SiF_{4(s)} + F$	1.0	
$SiO_{2(s)} + F \rightarrow SiF_{4(10)} + O_{2(10)}$	0.00015	
$C_{(s)} + F \rightarrow CF_{(s)}$	0.05	
$CF_{(s)} + F \rightarrow CF_{2(s)}$	0.045	
$CF_{2(s)} + F \rightarrow CF_{3(s)}$	0.03	
$CF_{3(s)} + F \rightarrow CF_{4(10)}$	0.0013	
$CF_{3(s)} + F \rightarrow CF_{4(s)}$	0.0087	
$CF_{4(s)} + F \rightarrow CF_{4(s)} + F$	1.0	
$SiO_2C_{(s)} + F \rightarrow SiO_2CF_{(s)}$	0.05	
$SiO_2CF_{(s)} + F \rightarrow SiO_2CF_{2(s)}$	0.045	
$SiO_2CF_{2(s)} + F \rightarrow SiO_2CF_{3(s)}$	0.03	
$SiO_2CF_{3(s)} + F \rightarrow SiO_{2(s)} + CF_{4(10)}$	0.0013	
$SiO_2CF_{3(s)} + F \rightarrow SiO_2CF_{4(s)}$	0.0087	
$SiO_2CF_{4(s)} + F \rightarrow SiO_2CF_{4(s)} + F$	1.0	
F_2 surface chemistry		
$PR_{(s)} + F_2 \rightarrow PR_{(s)} + F_2$	1.0	
$Si_{(s)} + F_2 \rightarrow SiF_{(s)}$	0.2	

$SiF_{(s)} + F_2 \rightarrow SiF_{2(s)}$	0.2	
$SiF_{2(s)} + F_2 \rightarrow SiF_{3(s)}$	0.154	
$SiF_{3(s)} + F_2 \rightarrow SiF_{4(10)}$	0.0056	
$SiF_{3(s)} + F_2 \rightarrow SiF_{4(s)}$	0.0544	
$SiF_{4(s)} + F_2 \rightarrow SiF_{4(s)} + F_2$	1.0	
$SiO_{2(s)} + F_2 \rightarrow SiF_{4(10)} + O_{2(10)}$	0.0003	
$C_{(s)} + F_2 \rightarrow CF_{(s)}$	0.1	
$CF_{(s)} + F_2 \rightarrow CF_{2(s)}$	0.1	
$CF_{2(s)} + F_2 \rightarrow CF_{3(s)}$	0.077	
$CF_{3(s)} + F_2 \rightarrow CF_{4(10)}$	0.0028	
$CF_{3(s)} + F_2 \rightarrow CF_{4(s)}$	0.0272	
$CF_{4(s)} + F_2 \rightarrow CF_{4(s)} + F_2$	1.0	
$SiO_2C_{(s)} + F_2 \rightarrow SiO_2CF_{(s)}$	0.1	
$SiO_2CF_{(s)} + F_2 \rightarrow SiO_2CF_{2(s)}$	0.1	
$SiO_2CF_{2(s)} + F_2 \rightarrow SiO_2CF_{3(s)}$	0.077	
$SiO_2CF_{3(s)} + F_2 \rightarrow SiO_{2(s)} + CF_{4(10)}$	0.0028	
$SiO_2CF_{3(s)} + F_2 \rightarrow SiO_2CF_{4(s)}$	0.0272	
$SiO_2CF_{4(s)} + F_2 \rightarrow SiO_2CF_{4(s)} + F_2$	1.0	
$C_{(10)}$ surface chemistry		
$PR_{(s)} + C_{(10)} \rightarrow PR_{(s)} + C_{(10)}$	1.0	
$Si_{(s)} + C_{(10)} \rightarrow Si_{(s)} + C_{(s)}$	1.0	
$SiF_{(s)} + C_{(10)} \rightarrow Si_{(s)} + CF_{(s)}$	1.0	
$SiF_{2(s)} + C_{(10)} \rightarrow SiF_{(s)} + CF_{(s)}$	0.41	
$SiF_{3(s)} + C_{(10)} \rightarrow SiF_{2(s)} + CF_{(s)}$	0.20	
$SiF_{4(s)} + C_{(10)} \rightarrow SiF_{4(s)} + C_{(10)}$	1.0	
$SiO_{2(s)} + C_{(10)} \rightarrow SiO_{2(s)}C_{(s)}$	0.1	
$C_{(s)} + C_{(10)} \rightarrow C_{(s)} + C_{(s)}$	0.66	
$CF_{(s)} + C_{(10)} \rightarrow C_{(s)} + CF_{(s)}$	0.66	
$CF_{2(s)} + C_{(10)} \rightarrow CF_{(s)} + CF_{(s)}$	0.272	
$CF_{3(s)} + C_{(10)} \rightarrow CF_{2(s)} + CF_{(s)}$	0.132	
$CF_{4(s)} + C_{(10)} \rightarrow CF_{4(s)} + C_{(10)}$	1.0	
$SiO_2C_{(s)} + C_{(10)} \rightarrow SiO_2C_{(s)} + C_{(s)}$	0.66	
$SiO_2CF_{(s)} + C_{(10)} \rightarrow SiO_2C_{(s)} + CF_{(s)}$	0.66	
$SiO_2CF_{2(s)} + C_{(10)} \rightarrow SiO_2CF_{(s)} + CF_{(s)}$	0.272	
$SiO_2CF_{3(s)} + C_{(10)} \rightarrow SiO_2CF_{2(s)} + CF_{(s)}$	0.132	
$SiO_2CF_{4(s)} + C_{(10)} \rightarrow SiO_2CF_{4(s)} + C_{(10)}$	1.0	
$CF_{(10)}$ surface chemistry		
$PR_{(s)} + CF_{(10)} \rightarrow PR_{(s)} + CF_{(10)}$	1.0	
$Si_{(s)} + CF_{(10)} \rightarrow Si_{(s)} + CF_{(s)}$	0.95	
$SiF_{(s)} + CF_{(10)} \rightarrow Si_{(s)} + CF_{2(s)}$	0.70	
$SiF_{2(s)} + CF_{(10)} \rightarrow SiF_{(s)} + CF_{2(s)}$	0.24	
$SiF_{3(s)} + CF_{(10)} \rightarrow SiF_{2(s)} + CF_{2(s)}$	0.12	

Reaction		
$SiF_{4(s)} + CF_{(10)} \rightarrow SiF_{4(s)} + CF_{(10)}$	1.0	
$SiO_{2(s)} + CF_{(10)} \rightarrow SiO_{2(s)}CF_{(s)}$	0.095	
$C_{(s)} + CF_{(10)} \rightarrow C_{(s)} + CF_{(s)}$	0.64	
$CF_{(s)} + CF_{(10)} \rightarrow C_{(s)} + CF_{2(s)}$	0.466	
$CF_{2(s)} + CF_{(10)} \rightarrow CF_{(s)} + CF_{2(s)}$	0.16	
$CF_{3(s)} + CF_{(10)} \rightarrow CF_{2(s)} + CF_{2(s)}$	0.08	
$CF_{4(s)} + CF_{(10)} \rightarrow CF_{4(s)} + CF_{(10)}$	1.0	
$SiO_2C_{(s)} + CF_{(10)} \rightarrow SiO_2C_{(s)} + CF_{(s)}$	0.64	
$SiO_2CF_{(s)} + CF_{(10)} \rightarrow SiO_2C_{(s)} + CF_{2(s)}$	0.466	
$SiO_2CF_{2(s)} + CF_{(10)} \rightarrow SiO_2CF_{(s)} + CF_{2(s)}$	0.16	
$SiO_2CF_{3(s)} + CF_{(10)} \rightarrow SiO_2CF_{2(s)} + CF_{2(s)}$	0.08	
$SiO_2CF_{4(s)} + CF_{(10)} \rightarrow SiO_2CF_{4(s)} + CF_{(10)}$	1.0	
$CF_{2(10)}$ surface chemistry		
$PR_{(s)} + CF_{2(10)} \rightarrow PR_{(s)} + CF_{2(10)}$	1.0	
$Si_{(s)} + CF_{2(10)} \rightarrow Si_{(s)} + CF_{2(s)}$	0.9	
$SiF_{(s)} + CF_{2(10)} \rightarrow Si_{(s)} + CF_{3(s)}$	0.4	
$SiF_{2(s)} + CF_{2(10)} \rightarrow SiF_{(s)} + CF_{3(s)}$	0.13	
$SiF_{3(s)} + CF_{2(10)} \rightarrow SiF_{2(s)} + CF_{3(s)}$	0.07	
$SiF_{4(s)} + CF_{2(10)} \rightarrow SiF_{4(s)} + CF_{2(10)}$	1.0	
$SiO_{2(s)} + CF_{2(10)} \rightarrow SiO_{2(s)}CF_{2(s)}$	0.090	
$C_{(s)} + CF_{2(10)} \rightarrow C_{(s)} + CF_{2(s)}$	0.6	
$CF_{(s)} + CF_{2(10)} \rightarrow C_{(s)} + CF_{3(s)}$	0.266	
$CF_{2(s)} + CF_{2(10)} \rightarrow CF_{(s)} + CF_{3(s)}$	0.086	
$CF_{3(s)} + CF_{2(10)} \rightarrow CF_{2(s)} + CF_{3(s)}$	0.046	
$CF_{4(s)} + CF_{2(10)} \rightarrow CF_{4(s)} + CF_{2(10)}$	1.0	
$SiO_2C_{(s)} + CF_{2(10)} \rightarrow SiO_2C_{(s)} + CF_{2(s)}$	0.6	
$SiO_2CF_{(s)} + CF_{2(10)} \rightarrow SiO_2C_{(s)} + CF_{3(s)}$	0.266	
$SiO_2CF_{2(s)} + CF_{2(10)} \rightarrow SiO_2CF_{(s)} + CF_{3(s)}$	0.086	
$SiO_2CF_{3(s)} + CF_{2(10)} \rightarrow SiO_2CF_{2(s)} + CF_{3(s)}$	0.046	
$SiO_2CF_{4(s)} + CF_{2(10)} \rightarrow SiO_2CF_{4(s)} + CF_{2(10)}$	1.0	
$CF_{3(10)}$ surface chemistry		
$PR_{(s)} + CF_{3(10)} \rightarrow PR_{(s)} + CF_{3(10)}$	1.0	
$Si_{(s)} + CF_{3(10)} \rightarrow Si_{(s)} + CF_{3(s)}$	0.85	
$SiF_{(s)} + CF_{3(10)} \rightarrow Si_{(s)} + CF_{4(s)}$	0.12	
$SiF_{2(s)} + CF_{3(10)} \rightarrow SiF_{(s)} + CF_{4(s)}$	0.04	
$SiF_{3(s)} + CF_{3(10)} \rightarrow SiF_{2(s)} + CF_{4(s)}$	0.016	
$SiF_{4(s)} + CF_{3(10)} \rightarrow SiF_{4(s)} + CF_{3(10)}$	1.0	
$SiO_{2(s)} + CF_{3(10)} \rightarrow SiO_{2(s)}CF_{3(s)}$	0.085	
$C_{(s)} + CF_{3(10)} \rightarrow C_{(s)} + CF_{3(s)}$	0.56	
$CF_{(s)} + CF_{3(10)} \rightarrow C_{(s)} + CF_{4(s)}$	0.08	
$CF_{2(s)} + CF_{3(10)} \rightarrow CF_{(s)} + CF_{4(s)}$	0.026	
$CF_{3(s)} + CF_{3(10)} \rightarrow CF_{2(s)} + CF_{4(s)}$	0.0106	

Reaction	Probability	
$CF_{4(s)} + CF_{3(10)} \rightarrow CF_{4(s)} + CF_{3(10)}$	1.0	
$SiO_2C_{(s)} + CF_{3(10)} \rightarrow SiO_2C_{(s)} + CF_{3(s)}$	0.56	
$SiO_2CF_{(s)} + CF_{3(10)} \rightarrow SiO_2C_{(s)} + CF_{4(s)}$	0.08	
$SiO_2CF_{2(s)} + CF_{3(10)} \rightarrow SiO_2CF_{(s)} + CF_{4(s)}$	0.026	
$SiO_2CF_{3(s)} + CF_{3(10)} \rightarrow SiO_2CF_{2(s)} + CF_{4(s)}$	0.0106	
$SiO_2CF_{4(s)} + CF_{3(10)} \rightarrow SiO_2CF_{4(s)} + CF_{3(10)}$	1.0	
$CF_{4(10)}$ surface chemistry		
$PR_{(s)} + CF_{4(10)} \rightarrow PR_{(s)} + CF_{4(10)}$	1.0	
$Si_{(s)} + CF_{4(10)} \rightarrow Si_{(s)} + CF_{4(s)}$	0.032	
$SiF_{(s)} + CF_{4(10)} \rightarrow SiF_{(s)} + CF_{4(s)}$	0.032	
$SiF_{2(s)} + CF_{4(10)} \rightarrow SiF_{2(s)} + CF_{4(s)}$	0.012	
$SiF_{3(s)} + CF_{4(10)} \rightarrow SiF_{3(s)} + CF_{4(s)}$	0.012	
$SiF_{4(s)} + CF_{4(10)} \rightarrow SiF_{4(s)} + CF_{4(10)}$	1.0	
$SiO_{2(s)} + CF_{4(10)} \rightarrow SiO_{2(s)}CF_{4(s)}$	0.032	
$C_{(s)} + CF_{4(10)} \rightarrow C_{(s)} + CF_{4(s)}$	0.032	
$CF_{(s)} + CF_{4(10)} \rightarrow CF_{(s)} + CF_{4(s)}$	0.032	
$CF_{2(s)} + CF_{4(10)} \rightarrow CF_{2(s)} + CF_{4(s)}$	0.012	
$CF_{3(s)} + CF_{4(10)} \rightarrow CF_{3(s)} + CF_{4(s)}$	0.012	
$CF_{4(s)} + CF_{4(10)} \rightarrow CF_{4(s)} + CF_{4(10)}$	1.0	
$SiO_2C_{(s)} + CF_{4(10)} \rightarrow SiO_2C_{(s)} + CF_{4(s)}$	0.032	
$SiO_2CF_{(s)} + CF_{4(10)} \rightarrow SiO_2CF_{(s)} + CF_{4(s)}$	0.032	
$SiO_2CF_{2(s)} + CF_{4(10)} \rightarrow SiO_2CF_{2(s)} + CF_{4(s)}$	0.012	
$SiO_2CF_{3(s)} + CF_{4(10)} \rightarrow SiO_2CF_{3(s)} + CF_{4(s)}$	0.012	
$SiO_2CF_{4(s)} + CF_{4(10)} \rightarrow SiO_2CF_{4(s)} + CF_{4(10)}$	1.0	
$CHF_{3(10)}$ surface chemistry		
$PR_{(s)} + CHF_{3(10)} \rightarrow PR_{(s)} + CHF_{3(10)}$	1.0	
$Si_{(s)} + CHF_{3(10)} \rightarrow Si_{(s)} + CF_{4(s)}$	0.027	
$SiF_{(s)} + CHF_{3(10)} \rightarrow SiF_{(s)} + CF_{4(s)}$	0.027	
$SiF_{2(s)} + CHF_{3(10)} \rightarrow SiF_{2(s)} + CF_{4(s)}$	0.011	
$SiF_{3(s)} + CHF_{3(10)} \rightarrow SiF_{3(s)} + CF_{4(s)}$	0.011	
$SiF_{4(s)} + CHF_{3(10)} \rightarrow SiF_{4(s)} + CHF_{3(10)}$	1.0	
$SiO_{2(s)} + CHF_{3(10)} \rightarrow SiO_{2(s)}CF_{4(s)}$	0.027	
$C_{(s)} + CHF_{3(10)} \rightarrow C_{(s)} + CF_{4(s)}$	0.027	
$CF_{(s)} + CHF_{3(10)} \rightarrow CF_{(s)} + CF_{4(s)}$	0.027	
$CF_{2(s)} + CHF_{3(10)} \rightarrow CF_{2(s)} + CF_{4(s)}$	0.011	
$CF_{3(s)} + CHF_{3(10)} \rightarrow CF_{3(s)} + CF_{4(s)}$	0.011	
$CF_{4(s)} + CHF_{3(10)} \rightarrow CF_{4(s)} + CHF_{3(10)}$	1.0	
$SiO_2C_{(s)} + CHF_{3(10)} \rightarrow SiO_2C_{(s)} + CF_{4(s)}$	0.027	
$SiO_2CF_{(s)} + CHF_{3(10)} \rightarrow SiO_2CF_{(s)} + CF_{4(s)}$	0.027	
$SiO_2CF_{2(s)} + CHF_{3(10)} \rightarrow SiO_2CF_{2(s)} + CF_{4(s)}$	0.011	
$SiO_2CF_{3(s)} + CHF_{3(10)} \rightarrow SiO_2CF_{3(s)} + CF_{4(s)}$	0.011	
$SiO_2CF_{4(s)} + CHF_{3(10)} \rightarrow SiO_2CF_{4(s)} + CHF_{3(10)}$	1.0	

CHF_3 surface chemistry		
$PR_{(s)} + CHF_3 \rightarrow PR_{(s)} + CHF_3$	1.0	
$Si_{(s)} + CHF_3 \rightarrow Si_{(s)} + CF_{4(s)}$	0.0027	
$SiF_{(s)} + CHF_3 \rightarrow SiF_{(s)} + CF_{4(s)}$	0.0027	
$SiF_{2(s)} + CHF_3 \rightarrow SiF_{2(s)} + CF_{4(s)}$	0.0011	
$SiF_{3(s)} + CHF_3 \rightarrow SiF_{3(s)} + CF_{4(s)}$	0.0011	
$SiF_{4(s)} + CHF_3 \rightarrow SiF_{4(s)} + CHF_3$	1.0	
$SiO_{2(s)} + CHF_3 \rightarrow SiO_{2(s)}CF_{4(s)}$	0.0027	
$C_{(s)} + CHF_3 \rightarrow C_{(s)} + CF_{4(s)}$	0.0027	
$CF_{(s)} + CHF_3 \rightarrow CF_{(s)} + CF_{4(s)}$	0.0027	
$CF_{2(s)} + CHF_3 \rightarrow CF_{2(s)} + CF_{4(s)}$	0.0011	
$CF_{3(s)} + CHF_3 \rightarrow CF_{3(s)} + CF_{4(s)}$	0.0011	
$CF_{4(s)} + CHF_3 \rightarrow CF_{4(s)} + CHF_3$	1.0	
$SiO_2C_{(s)} + CHF_3 \rightarrow SiO_2C_{(s)} + CF_{4(s)}$	0.0027	
$SiO_2CF_{(s)} + CHF_3 \rightarrow SiO_2CF_{(s)} + CF_{4(s)}$	0.0027	
$SiO_2CF_{2(s)} + CHF_3 \rightarrow SiO_2CF_{2(s)} + CF_{4(s)}$	0.0011	
$SiO_2CF_{3(s)} + CHF_3 \rightarrow SiO_2CF_{3(s)} + CF_{4(s)}$	0.0011	
$SiO_2CF_{4(s)} + CHF_3 \rightarrow SiO_2CF_{4(s)} + CHF_3$	1.0	

S2. Brief description of the SiO_2 etch mechanism

The surface chemistry set is based on five fundamental mechanisms:

- Physical sputtering, i.e. the removal of substrate material by energetic inert ions, in this case Ar^+.
- Chemical etching, i.e. the removal of substrate material by reactive neutrals. For instance, SiO_2 can be removed in the form of the molecules SiF_4 and O_2, after interaction with F and F_2. This reaction is, however, less effective than chemical etching of a Si substrate with F and F_2.
- Deposition, i.e. the attachment of a plasma particle on the surface. The plasma particle can be a molecule (e.g. physisorption of CF_4 or CHF_3), a radical (e.g. chemisorption of F or CF_x, with x = 0,…,3), an etch product (e.g. sputtered SiO_2) or a reactive ion (e.g. deposition of CF_x^+, with x = 1,…,3).
- Direct reactive ion etching, i.e. the removal of substrate material by reactive ions. CF_x^+ ions (with x = 1,…,3) are particularly effective at removing SiO_2, because their carbon atom can bind with the oxygen in the substrate to form O_2, while their fluorine atoms can bind with the silicon in the substrate to form SiF_4 molecules or SiF_x radicals. The kinetic energy of the ion provides the activation energy required for the reaction and the emission of the reaction products.
- Ion-assisted chemical etching, i.e. the removal of substrate material and deposited material combined by energetic ions. CF_4 and CHF_3 molecules and CF_x radicals, for example, provide the necessary carbon and fluorine components to combine with the SiO_2 substrate for the formation of O_2 and SiF_x products, but this reaction still requires an activation energy. This can be provided by the kinetic energy of an incident ion, such as Ar^+.

At the conditions used in the present study, ion-assisted chemical etching forms the most dominant etch mechanism in the simulations, as shown in Ref. [1]. Direct reactive ion etching contributes to the etch rate

on the second place. The other mechanisms have a much lower effect on the etch rate, but can significantly influence the etched profile.

References

1. Vanraes, P., S. Parayil Venugopalan, and A. Bogaerts, *Multiscale modeling of plasma–surface interaction—General picture and a case study of Si and SiO2 etching by fluorocarbon-based plasmas.* Applied Physics Reviews, 2021. **8**(4): p. 041305.